

Influence of tunable interfaces on radiation tolerance and nanomechanical behavior of homogeneous multi-nanolayered Al_{1.5}CoCrFeNi high entropy alloy films



Guo Pu^a, Liwei Lin^a, Ding Ren^a, Kefu Gan^c, Bin Liu^{b,*}, Zongbiao Ye^a, Yihan Wang^a, Kun Zhang^a, Zhiming Li^{b,c}, Bo Liu^{a,*}

^a Key Laboratory of Radiation Physics and Technology of Ministry of Education, Institute of Nuclear Science and Technology, Sichuan University, Chengdu 610064, China

^b Powder Metallurgy Research Institute, Central South University, Changsha 410083, China

^c School of Materials Science and Engineering, Central South University, Changsha 410083, China

ARTICLE INFO

Article history:

Received 23 December 2021

Revised 23 March 2022

Accepted 16 April 2022

Available online 22 April 2022

Keywords:

High entropy alloy films
Multi-nanolayers

Interface

Helium ion irradiation

Swelling

Nano-mechanical properties

ABSTRACT

Introducing high-density defect sinks, e.g., grain boundaries (GBs) and interfaces, to capture helium (He) atoms and irradiation-induced defects under He⁺ irradiation is a promising strategy for constructing novel nuclear-materials with enhanced radiation tolerance. To understand the vital roles of GBs and interfaces on the irradiation response in high entropy alloys (HEAs), high-density GBs and homogeneous interfaces between layers were firstly introduced into multi-nanolayered Al_{1.5}CoCrFeNi HEA films by tailoring the nominal monolayer thickness (*h*) ranging from 2 to 100 nm. The multi-nanolayered HEA films were then irradiated by 60 keV He⁺ at a fluence of $1 \times 10^{17} \text{ cm}^{-2}$. The results show that the He bubbles with size of 1–2 nm were preferentially distributed along the GBs within the films and the phase structure kept stable in the irradiated HEA films with less interfaces (such as *h* = 10 nm). This suggests that the He bubbles mainly distributed at GB sinks due to the high-density GB intersections acted as dominant defect-sinks to trap He atoms. While both the distribution of He bubbles throughout the interfaces and the partial BCC→FCC phase transformation due to radiation-induced segregation were disclosed by introducing numerous interfaces in the irradiated multi-nanolayered HEA films (*h* = 10 and 30 nm). The corresponding intrinsic mechanism of He behavior was elucidated based on the interactions between the He defects and the nano-GBs or homogeneous interfaces. The underlying mechanisms of irradiation-induced phase transformation were explained by the relief of compression stress and the radiation-induced segregation behavior by vacancy-flux. Also, the roles of interfaces and GBs on the irradiation swelling and nano-mechanical properties of the HEA films were also revealed by the systematic investigations.

© 2022 Elsevier B.V. All rights reserved.

1. Introduction

Considering the harsh operating-environments of future reactor system, exploring advanced nuclear-materials with superior comprehensive-performance is a pivotal mission to overcome the susceptibility to failure under particle irradiation [1]. The emerging high entropy alloys (HEAs) composed of multiple principal elements have elicited widespread attention on account of their unique compositional design, tunable micro-structures and favorable mechanical properties [2–5]. Recently, a number of experimental and computational studies have revealed that some HEAs

possess extraordinary radiation tolerance compared to the conventional steels and alloys [6–10]. In general, the extensive production of helium (He) atoms caused by the (n, α) nuclear transmutation reaction can be precipitated into nano-meter gas bubbles in conventional alloys, acting as preferred sites for He bubble nucleation and growth [11,12]. The aggregated He bubbles generate severe volume swelling and degrade the mechanical performance of the materials in nuclear reactor. For the novel HEAs which have fundamental differences with the conventional alloys, it has been a promising topic to explore the potential enhancement of radiation tolerance and the interactions between the multiple principal elements and the He atoms under irradiation.

In recent years, numerous efforts have been performed to explore He damage behavior and defect evolution in the coarse-

* Corresponding authors.

E-mail addresses: binliu@csu.edu.cn (B. Liu), liubo2009@scu.edu.cn (B. Liu).

grained bulk HEAs [13–17]. Yang et al. [15] revealed that the size of He bubbles in the CrMnFeCoNi HEA is significantly smaller than that in the pure Ni and 304 austenitic stainless steel under the same condition of He ion irradiation, and this was ascribed to the special high entropy effect and the prominent sluggish diffusion effect in HEAs. Chen et al. [16] showed that the He atoms were easier to be trapped by nucleated He bubbles, promoting the growth of He bubbles in the FeCoCrNi HEA. Also, the energetic He^+ induced faulted interstitial Frank dislocation loops with Burgers vector $1/3\langle 111 \rangle$ were detected in the matrix of crystalline FeCoNiCrTi_{0.2} HEA with a low stacking fault energy (SFE) [17]. The evolution of He bubbles and dislocation loops, which are caused by the supersaturation of vacancies and self-interstitial atoms, would accelerate solute diffusion and thus drive the element segregation toward a new equilibrium state in the irradiated alloys. It was also found that the elemental enrichment or depletion in coarse-grained CoCrFeMnNi HEA and the phase instability in Al_{1.5}CrFeNi HEA can be induced by the dislocation loops and the accumulated vacancy-type defects at irradiation damage region owing to the radiation-induced segregation (RIS) [18–19]. Based on these recent works, it is crucial to explore novel strategies to design HEAs with further enhanced ability to mitigate radiation-induced defects so as to control the nucleation-growth of He bubbles and weaken the RIS or phase decomposition behavior.

As previously established, nano-crystals in metals and alloys exhibit an outstanding radiation tolerance compared with their coarse-grained counterparts owing to their high-density grain boundary (GB) sinks. The high-density GBs provide diffusion channels for the migration of He atoms, these GB sinks are capable of absorbing radiation-induced defects (He interstitials and vacancies) as well as blocking the migration of defects to form dislocation loops and complex extended defects [20–22]. In our previous work, we achieved high-density GBs in nanocrystalline Al_{1.5}CoCrFeNi HEA films and showed that the He clusters were preferentially distributed at GB sinks rather than inside grains [23]. To provide more defect sinks for He trapping, many other studies also proposed that the construction of heterogeneous phase interfaces, such as those in W/Cu [24], Nb/Cu [25] and FeCoCrNi/Cu [26] multi-nanolayered films, exhibited excellent annihilation-ability of He defect owing to the contribution coming from great interfacial effect. However, He bubbles in the incoherent phase interfaces tend to diffuse and migrate into the other phase (such as Cu phase) because of its lower surface energy, which seriously expedites He bubble growth in the second phase and weakens the mechanical properties [24–26]. To date, there is practically nothing known about the irradiation resistance behavior of multi-nanolayered single-phase HEA films containing both nano-crystals and homogeneous interfaces. Also, the dominated competitive relationships between GBs and multi-nanolayered interfaces in improving the He^+ radiation resistance are not elucidated for the tailored homogeneous multi-nanolayered HEA films. In comparison with the heterogeneous phase interface, the homogeneous interface in multi-nanolayered single-phase HEA film has abundant defect sinks, such as vacancies and interstitials [27], which are resulted from the lattice distortion and the multiple principal elements. The numerous interfaces may not only provide defect sinks to annihilate the irradiation-induced defects and He atoms, but also effectively minimize the interface mismatch and irradiation-induced stress. In this regard, the investigation of homogeneous multi-nanolayered HEA films can provide new perspectives on designing novel nuclear-materials and understanding the fundamental irradiation behavior.

In this work, both high-density GBs and homogeneous multi-nanolayered interfaces were firstly introduced into the Al_{1.5}CoCrFeNi HEA nano-films by adjusting the nominal mono-layer thickness (h) ranging from 2 to 100 nm. The multi-nanolayered HEA films produced via radio frequency (RF) magnetron sputter-

ing were irradiated by 60 keV He^+ ion beam at a fluence of $1 \times 10^{17} \text{ cm}^{-2}$. We found that the He bubbles were formed mainly within the nano-crystals in HEA films of $h = 2$, 100 nm due to the dominant effect of high-density GBs in these cases. On the other hand, diverse He bubbles in the multi-nanolayered Al_{1.5}CoCrFeNi HEA films of $h = 10$, 30 nm were observed at the homogeneous multi-nanolayered interfaces. This discovery suggests that the abundant interfaces play a vital role in facilitating the growth of He bubbles, demonstrating a inverse results with previous heterogeneous-interface modeling that the heterogeneous multilayers interface can notably suppress the formation of large-scale He bubble [24,25]. The correlation of phase structure with tailored thickness of each layer in the multi-nanolayered HEA films was investigated systematically. The corresponding intrinsic mechanism of structural evolution was also discussed based on the interaction between He defects and GBs or interface sinks. This study provides new insights into the understanding of controlling defect production, migration, aggregation as well as structure evolution. Also, the present work showed that the swelling is higher and the hardening is lower in the multi-nanolayered HEA films with homogeneous interfaces compared to that in the HEA films with high-density GBs. The corresponding mechanisms behind the swelling and hardening behavior of these HEA films were also discussed in detail.

2. Experimental details

The homogeneous multi-nanolayered Al_{1.5}CoCrFeNi HEA films were deposited by RF magnetic sputtering technique at room temperature on the single-crystalline silicon (Si) substrates, which were ultrasonically cleaned by acetone and alcohol, respectively. The chamber was evacuated to a background pressure lower than $6 \times 10^{-4} \text{ Pa}$ before HEA film deposition, and pure Ar with a flow rate of 35 sccm was introduced to provide the deposition pressure of 0.45 Pa. The sputtering target composed of Al_{1.5}CoCrFeNi was fabricated by powder metallurgy with high purity (>99.99%, weight percent) raw materials of aluminum, cobalt, chromium, iron and nickel powders. The deposition power was controlled at 110 W. The multi-nanolayered Al_{1.5}CoCrFeNi HEA films were obtained by regulating the nominal mono-layer thickness ranging from 2 to 100 nm (namely, $h = 2$, 10, 30 and 100 nm). The mono-layer thickness was constructed by alternately disrupting Ar flux during deposition process according to the fixed deposition time of each lamellae. The nominal thickness of the all multi-nanolayered Al_{1.5}CoCrFeNi HEA films was about 300 nm. During the deposition, the sample holder rotated at a speed of 20 rpm to keep the composition uniformity of these films. All the as-deposited samples were irradiated with 60 keV He^+ ion-beam, at a fluence and a fluence rate of $1 \times 10^{17} \text{ cm}^{-2}$ and $5.56 \times 10^{13} \text{ cm}^{-2}\cdot\text{s}^{-1}$, respectively. These as-deposited samples were mounted on a water-cooled holder, the environment temperature in chamber was about 300 K detected by thermocouple thermometer during He^+ bombardment samples.

Grazing Incidence X-ray Diffraction (GIXRD, RigakuDmax 2000) with a Cu $K\alpha$ radiation wavelength of 0.15418 nm was carried out to characterize the phase structure for the multi-nanolayered Al_{1.5}CoCrFeNi HEA films before and after irradiation, the GIXRD data were recorded at a grazing incidence angle of 2° for the angle scanning range of 20°–80° with a step of 0.01° and a dwell time of 4 s for each step. The displacements per atom (DPA) and the He concentration as a function of depth were calculated by SRIM-2013 with the full cascade TRIM simulation as the Al_{1.5}CoCrFeNi HEA is multi-elemental target [28], using the threshold displacement energies of 25 eV for Al atom and of 40 eV for other atoms as well as the Al_{1.5}CoCrFeNi HEA density at 6.2449 g/cm³ [29,30]. Irradiation damage DPA and He concentration (in at. %) were calculated from

the SRIM's output files by the following equations [31]:

$$\left(\frac{\overbrace{\text{vacancy.txt}}^{\text{vacancies}}}{\text{ions} \times \text{\AA}^3} \right) \times \left(\frac{10^8 \left(\frac{\text{\AA}}{\text{cm}} \right) \times \text{Fluence} \left(\frac{\text{ions}}{\text{cm}^2} \right)}{7.78 \times 10^{22} \left(\frac{\text{atoms}}{\text{cm}^3} \right)} \right) = \left(\frac{\# \text{vacancies}}{\text{atom}} \right) = \text{DPA} \quad (1)$$

$$\left(\frac{\overbrace{\text{range.txt}}^{\text{atom}/\text{cm}^3}}{\text{atoms}/\text{cm}^2} \right) \times \left(\frac{\text{Fluence} \left(\frac{\text{ions}}{\text{cm}^2} \right)}{7.78 \times 10^{22} \left(\frac{\text{atoms}}{\text{cm}^3} \right)} \right) \times 100 = \text{at.\%} \quad (2)$$

The micro-graph of surface and cross-sectional image of the as-deposited HEA film were characterized by the Scanning Electron Microscope (SEM, JEOL, JSM 7500F) and Transmission Electron Microscope (TEM, Tecnai G² F20), respectively. The profiles of radiation-induced defects and He bubbles were detected by through-focused bright field TEM (BF-TEM) imaging. The Selected Area Electron Diffraction (SAED) was performed to characterize the micro-structures of multi-nanolayered Al_{1.5}CoCrFeNi HEA films after He⁺ irradiation. The cross-sectional TEM foils from the HEA films were prepared by mechanical polishing, followed by ion milling to form a wedge to create sufficient electron transparency on a Gatan precision ion polishing system. A combination of the Rutherford Backscattering Spectrometry (RBS) and Scanning TEM-Energy Dispersive Spectroscopy (STEM-EDS, FEI F200X Talos) was carried out to comprehensively analyze the RIS behavior of the irradiated multi-nanolayered films. RBS experiments were performed by using 2 MeV ⁴He ion beam, the RBS spectrum were analyzed with RUMP program.

The height profile difference ΔH between the irradiated and masked regions (unirradiated) can be measured by Atomic Force Microscope (AFM). The irradiation-induced swelling and swelling rate in irradiated HEA films were determined based on the analysis results of AFM and SRIM calculation to investigate the irradiation-induced volume changes of these films. Nanoindentation was carried out with a Nano Indenter G200x (American KLA Corporation) using continuous stiffness measurement (CSM) method. The dynamic frequency was 110 Hz and the loading resolution was 15 mN. The indent depth is about 50 nm which is only one fifth of the irradiated peak depth, the shallow impression effectively eliminates the influence of underlying matrix (non-damaged region) due to the indentation size effects. The measurements of both hardness and elastic modulus as a function of indentation depth were obtained, extracting average hardness and elastic modulus at damage depth of 50–250 nm. And at least fifteen indents were measured for each sample to get average values and standard deviation.

3. Results

3.1. Micro-structure of as-deposited multi-nanolayered HEA films

Fig. 1(a) shows the GIXRD patterns of as-deposited multi-nanolayered Al_{1.5}CoCrFeNi HEA films with nominal mono-layer thicknesses ($h = 2, 10, 30$ and 100 nm). The as-deposited HEA films with various h can be indexed as a body centered cubic (BCC) single-phase structure because Al atoms molar ratio is increased to 1.5 [32]. With the increasing h , BCC (110) peak gradually becomes stronger, reaching the maximum for the HEA film of $h = 100$ nm because of the increased thickness h . At the same time, the (110) peak slightly shifts to a lower diffraction angle, which indicates the decreased contraction of lattice planar spacing. **Fig. 1(b)** shows

the surface morphology and inserted cross-sectional TEM image of as-deposited Al_{1.5}CoCrFeNi HEA film with $h = 10$ nm, revealing that the as-deposited HEA film has a uniform surface morphology and obvious lamellar-structure. The homogeneous-interface in the multi-nanolayered Al_{1.5}CoCrFeNi HEA film may root in the lattice distortion and/or disorder. Neither cracks nor exfoliation are observed between the substrate and interface from the SEM and inserted TEM images, indicating that a well interfacial bond and a high deposition quality were obtained by reducing the interface mismatch.

3.2. Micro-structure and He behavior of irradiated multi-nanolayered HEA films

The DPA and He concentration were calculated as a function of depth by SRIM-2013. As shown in Fig. S1 (Supplementary Information), the He concentration and DPA profiles with the depth present roughly Gaussian-like distribution, the damage peak region is approximately located at 250 nm in depth from the surface of samples, in which the calculated maximum values of DPA and He concentration are about 7.01 dpa and 7.42 at.% at fluence of $1 \times 10^{17} \text{ cm}^{-2}$, respectively. **Fig. 2(a)** displays the cross-sectional morphology of the multi-nanolayered film with nominal monolayer thickness of 2 nm irradiated at fluence of $1 \times 10^{17} \text{ cm}^{-2}$. The invisible lamelletted interface can be observed from the **Fig. 2(a)**, the interior interfaces may be broken down by the epitaxial growth of nano-crystal during the alternating deposition of each lamellae. **Fig. 2(b)–(d)** show the BF-TEM images of multi-nanolayered HEA films with $h = 10$ nm, 30 and 100 nm, respectively. Numerous spherical and elliptic He bubbles with ribbon-like structure are formed at the distinct interfaces (marked by red arrows in the figures). The bubble sizes of 3–4 nm in films of $h = 10$ nm and 30 nm are larger than the bubble sizes (1–2 nm) in films of $h = 2$ and 100 nm.

Fig. 3 shows the corresponding enlarged HRTEM images, respectively. Partial grains (marked by dash line) with average sizes about 5–6 nm can be observed from the enlarged HRTEM image in **Fig. 3(a)**. Isolated He bubbles in the matrix, as well as He bubbles decorating GBs and dislocations are observed. He bubbles with ribbon-like structure are formed by the He-vacancy aggregation at GBs, indicating that the diffusion occurs readily along GBs and dislocations by a pipe diffusion mechanism. Moreover, the amorphous regions (shown in inserted Fast Fourier Transform (FFT) and inverse FFT image) are induced by the accumulated He bubbles and irradiated defects, such as <110> dislocations and interstitial-type defects, etc. As shown in the **Fig. 3(b)**, the ribbon-like He bubbles are formed by numerous spherical and elliptic bubbles at the interfaces (marked by red arrows in the figures). At the same time, less bubbles are observed in the grains of the Al_{1.5}CoCrFeNi HEA films due to the coexistence of nano-crystals and multi-nanolayered interfaces, indicating that the introduced He atoms in matrix are mainly migrated into the interfaces through GB channels. With increasing h to 30 nm, the similar ribbon-like distribution of He bubble is also observed at the interfaces, as shown in **Fig. 3(c)**. In addition to the formation of He bubble at the interfaces, more He bubbles (marked by red arrows) are formed inside the each-lamellae, this is due to the increase of diffusion distance of He atoms. The residuary He atoms in each-layers are captured rapidly by the GBs in lamellae matrix, then these He atoms are further aggregated to form bubbles in each lamellae. With increasing the individual-layer thickness from 10 to 30 nm, the diffusion distance is considerably enhanced for He interstitial or vacancy defects to diffusion from the original location to nearest interface sinks, enabling the rapid diffusion of He atoms before transforming into relatively stable aggregation in each lamellae [24–26]. The amorphous regions are also induced in the damage peak region in these multilayered

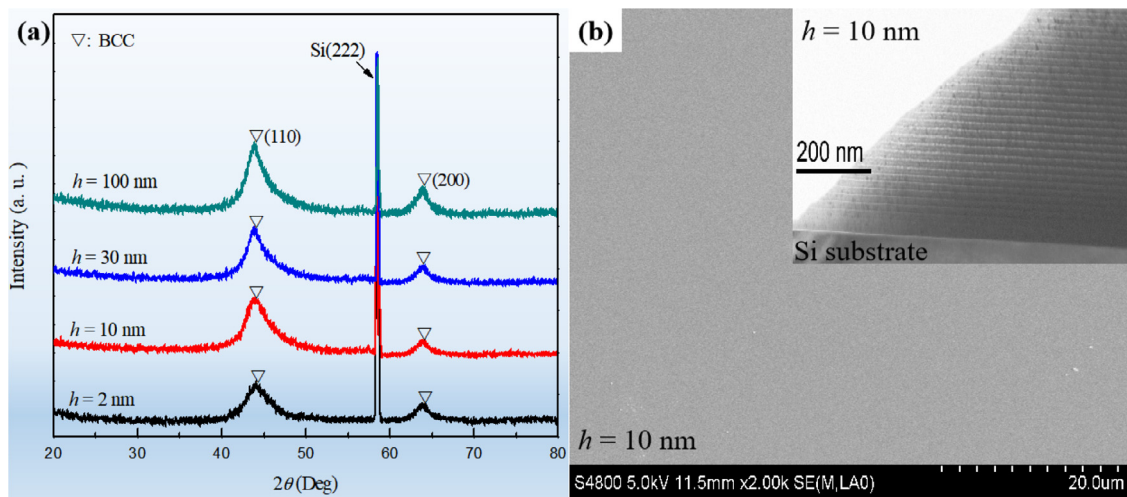


Fig. 1. (a) GIXRD patterns of the as-deposited Al_{1.5}CoCrFeNi HEA multilayer films with nominal monolayer thicknesses ($h = 2, 10, 30$ and 100 nm); (b) the surface morphology and inserted cross-sectional TEM image of as-deposited Al_{1.5}CoCrFeNi HEA film with the monolayer thickness of 10 nm.

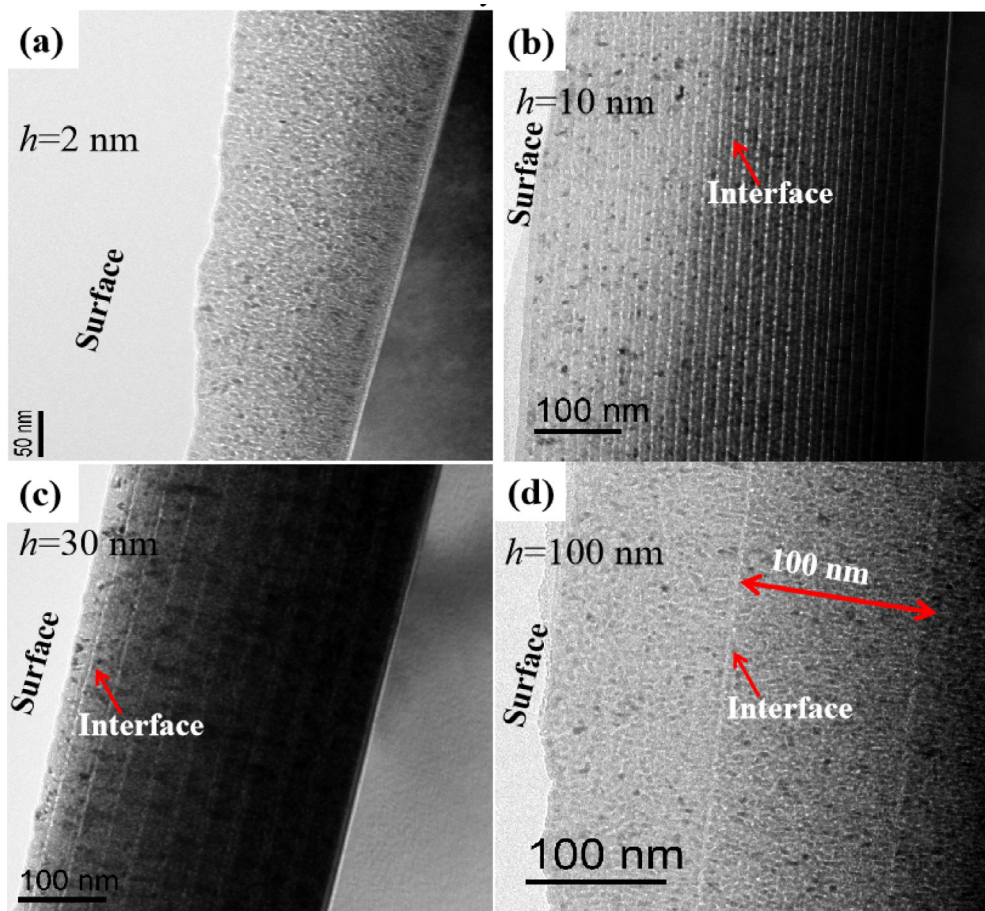


Fig. 2. Cross-sectional micro-structure of multi-nanolayered Al_{1.5}CoCrFeNi HEA films ((a) $h = 2$ nm, (b) 10 nm, (c) 30 nm and (d) 100 nm) irradiated by He⁺ at room temperature with fluence of 1×10^{17} cm⁻².

films (as shown in rectangle). Nano-crystals (as shown in the inserted FFT and IFFT images) with sizes of 5–6 nm are observed in the films of $h = 10$ nm and 30 nm from each-lamellae in the HRTEM images. The artificially introduced interfaces increase the capturing ability of He atoms and the annihilation of irradiation defects, which are helpful to maintain the stability and integrity of nano-crystal.

Abnormal He behavior is observed when the monolayer thickness is further increased to 100 nm. As shown in the Fig. 3(d), the interface numbers are reduced and GB intersections are increased significantly in the each lamellae. It is interesting to note that the bubbles are also decorated at the interfaces and GBs, a similar bubble size and distribution feature can be observed compared with the irradiated HEA film of $h = 2$ nm. In contrast to the bubble

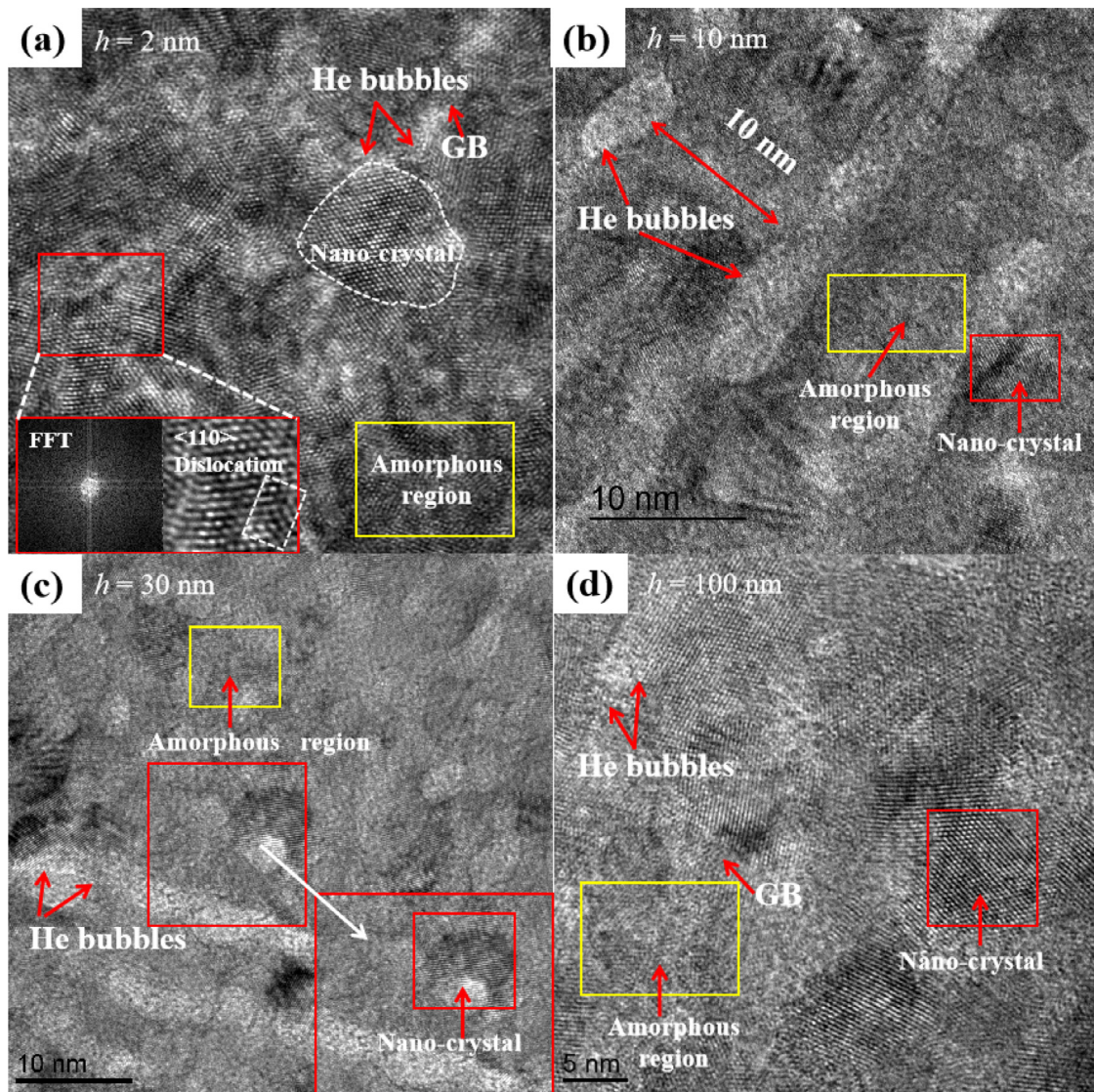


Fig. 3. Enlarged HRTEM images of multi-nanolayered $\text{Al}_{1.5}\text{CoCrFeNi}$ HEA films ((a) $h = 2 \text{ nm}$, (b) $h = 10 \text{ nm}$, (c) $h = 30 \text{ nm}$ and (d) $h = 100 \text{ nm}$) irradiated by He^+ at room temperature with fluence of $1 \times 10^{17} \text{ cm}^{-2}$.

size in HEA film of $h = 10$ and 30 nm , significantly reduced size is observed inside film matrix or the limited interfaces due to the obviously augmented distance for He diffusion and the sluggish diffusion nature of He-vacancy defects in HEA. Therefore, the introduced He atoms are captured preferentially by the high-density GBs on account of the higher GBs-to-interfaces ratio in the multi-nanolayered film ($h = 100 \text{ nm}$), the enhanced GB intersections act as dominant defect sinks, which should be responsible for the dispersed distribution of He bubble.

3.3. Phase structure of irradiated multi-nanolayered HEA films

Fig. 4(a) shows the variation in the GIXRD spectra of $\text{Al}_{1.5}\text{CoCrFeNi}$ HEA multi-nanolayered films irradiated with 60 keV He^+ at fluence of $1 \times 10^{17} \text{ cm}^{-2}$. It is found that the phase composition is BCC single-phase structure, no extra diffraction peaks appear in the samples with $h = 2$ and 100 nm , indicating that the phase structure presents relatively stable in the samples of $h = 2$ and 100 nm . However, except for the BCC diffraction peaks, FCC (111), FCC (200) and FCC (220) diffraction peaks can be also observed in the samples of $h = 10 \text{ nm}$ and 30 nm , respectively, sug-

gesting that the partial BCC \rightarrow FCC phase transformations are induced by He^+ irradiation in these multi-nanolayered HEA films. M. Barr et al. [33] detected the RIS behavior at high angle grain boundaries in CoCrFeNiMn HEA under irradiation damage level of 2–3 dpa. The RIS behavior is known to be a micro-structure evolution in the formation of secondary phases [20]. Therefore, it may be predicted that the interaction of irradiation defects and interfaces in the tunable multi-nanolayered $\text{Al}_{1.5}\text{CoCrFeNi}$ HEA films ($h = 10, 30 \text{ nm}$) would induce the segregation of alloying elements and lead to the instability of phase structure under this damage level. Furthermore, small peak shifts are observed in the fitting curves of Fig. 4(b), the enlarged part of Fig. 4(a). The peak positions of FCC (111) and BCC (110) peaks in the samples with $h = 10 \text{ nm}$ and 30 nm continuously shift to higher diffraction angles. It suggests the decrease of corresponding interplanar distance for each lamellae after irradiation, the lattice shrinkage is believed to result from residual compression-stress, which is induced by the bubble growth at interfaces [26].

In order to further clarify the existence of irradiation-induced residual stress, the relative change in lattice parameters ($\Delta a/a$) and unit cell volume ($\Delta V/V, V = a^3$) of the films before and af-

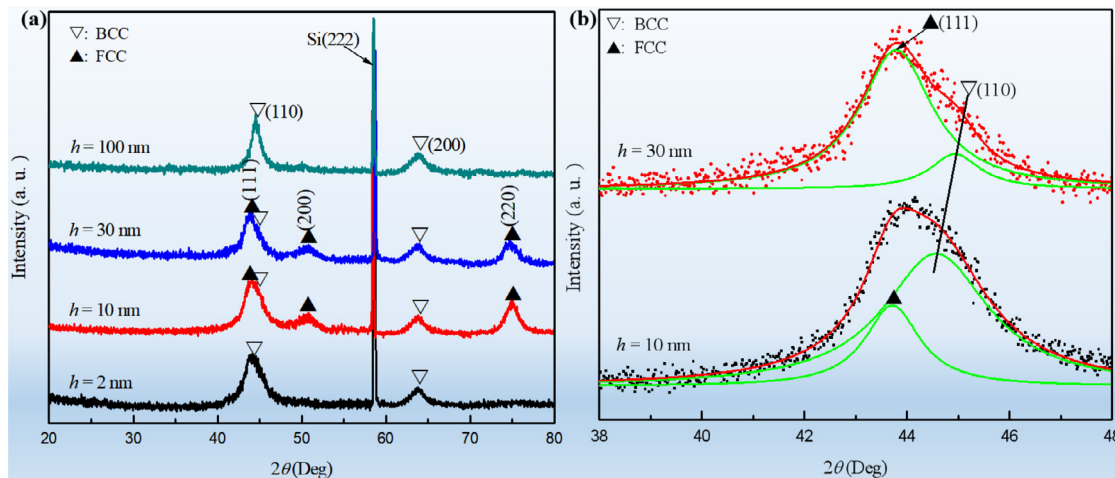


Fig. 4. (a) GIXRD patterns of irradiated $\text{Al}_{1.5}\text{CoCrFeNi}$ HEA multi-nanolayered films with nominal monolayer thicknesses ($h = 2, 10, 30$ and 100 nm); (b) the enlarged patterns and fitting curves are obtained from (a), the phase transformation in multi-nanolayered HEA film of $h = 10$ nm and $h = 30$ nm is evidenced after He^+ irradiation.

Table 1

The relative change in lattice parameters and unit cell volume of irradiated $\text{Al}_{1.5}\text{CoCrFeNi}$ HEA films with different h .

Monolayer thickness h (nm)	$\Delta a/a$ (%)	$\Delta V/V$ (%)
2	0.37	0.093
10	-11.02	-2.74
30	-15.81	-3.92
100	0.76	0.194

ter irradiation were analyzed from BCC (110) peak in the GIXRD patterns, as shown in Table 1. For the films with $h = 2$ nm and 100 nm, $\Delta a/a$ and $\Delta V/V$ are positive values, indicating that the irradiated HEA films exhibit slight expansion in lattice due to the dispersed distribution of He bubbles. Nevertheless, the $\Delta a/a$ and $\Delta V/V$ present negative values in the films with $h = 10$ nm and 30 nm, suggesting that the lattice shrinkage inside each lamellae results from the squeezing of residual compression-stress, which is induced by the bubble aggregation at each interface, it's well agreement with the analysis result in Fig. 4(b). The irradiation-induced residual compression-stress may act as driving force to promote the composition reorganization and phase transformation.

Fig. 5 shows the SAED patterns of irradiated HEA multi-nanolayered films. SAED patterns are obtained from the damage peak regions (the depth rang of ~ 200 nm) to further certificate the phase evolution. As illustrated in Fig. 5(a), it is found that a brightest diffraction ring and other fainter diffraction rings are observed in the SAED patterns, the fainter diffraction rings are formed due to the lattice disorder regions (shown in Fig. 3(a) and (d)). Besides, there is not any extra diffraction ring arising from the BCC matrix, indicating that the film of $h = 2$ nm maintains the phase stability after He^+ irradiation. The nanoscale grain is formed in the HEA film (as shown in Fig. 3(a)), suggesting that the nano-crystalline HEA film ($h = 2$ nm) is conducive to the phase stability. As the individual layer thickness of multi-nanolayered HEA films increased to $h = 10$ nm and 30 nm, the FCC (111), FCC (200) and FCC (220) diffraction rings appear in the SAED patterns of Fig. 5(b) and (c), respectively, this characterized results basically are consistent with the GIXRD patterns. As the h is increased to 100 nm, only the diffraction rings of the BCC phase structure can be observed in the Fig. 5(d), indicating that the drastic reduction of the interface is responsible for the phase stability in the irradiated $\text{Al}_{1.5}\text{CoCrFeNi}$ HEA film. The effects of interface on the phase stability in these HEA films are investigated by detecting the RIS to reveal the under-

lying mechanism of phase transformation in the following detailed analysis.

Fig. 6 shows the HRTEM images of multi-layered HEA films of $h = 10$ nm and $h = 30$ nm, in which both nano-crystalline structure and irradiation-induced amorphous regions are observed near the interface. Irradiation-induced amorphous regions are further presented in HRTEM images. The d -spacing ($d_{\text{BCC}(110)} = 0.1994$ nm, $d_{\text{FCC}(200)} = 0.2008$ nm) and corresponding grain orientation are given in the inserted FFT and IFFT images (Fig. 6(a)), which are transformed from the HRTEM image of the damage peak region of film of $h = 10$ nm (shown in red rectangles). For the multilayered HEA film of $h = 30$ nm, the d -spacing ($d_{\text{BCC}(110)} = 0.1993$ nm, $d_{\text{FCC}(111)} = 0.1991$ nm) are also calculated in the inserted IFFT images (Fig. 6(b)). Additionally, the phase interfaces between the BCC and FCC phase are also shown in these HEA multilayered films (marked by the white rectangles), indicating that the partial BCC \rightarrow FCC phase transformations are induced by He^+ irradiation in these multi-nanolayered HEA films, the phase transformation mechanism will be discussed in the following paragraph.

3.4. Radiation induced segregation (RIS) in irradiated multi-nanolayered HEA films

The new phases nucleation and growth were induced by RIS when the concentration of solute atoms at the sinks exceeds the solubility in the alloy [19, 34–35]. The RBS spectra and their simulated results of the irradiated HEA film are shown in Fig. 7. The plateaus or peaks represent the redistribution of the constituting elements, which corresponds to the total backscattering signals of 2 MeV ${}^4\text{He}$ ions from alloy atoms in crystals of irradiated HEA films. As shown in Fig. 7(a), the constituting elements in HEA film keep a stable distribution. In contrast, several salient peaks are detected in the films of $h = 10$ nm and 30 nm, the corresponding peaks show the constituting elements content redistribution or alloy element enrichment in HEA films (shown in Fig. 7(b) and (c)), in which the detailed element component could not be fully distinguished from the analysis spectra due to the approximate nucleus and different metal atoms take up lattice positions randomly. The similar weak peaks are observed in the sample of $h = 100$ nm (Fig. 7(d)), suggesting that the constituting elements are also reorganized slightly due to the RIS effect due to the limited interface-numbers. The different tendencies of RBS spectra qualitatively analyze the irradiation-induced composition enrichment. The detailed composition distribution was further characterized by STEM-EDS maps.

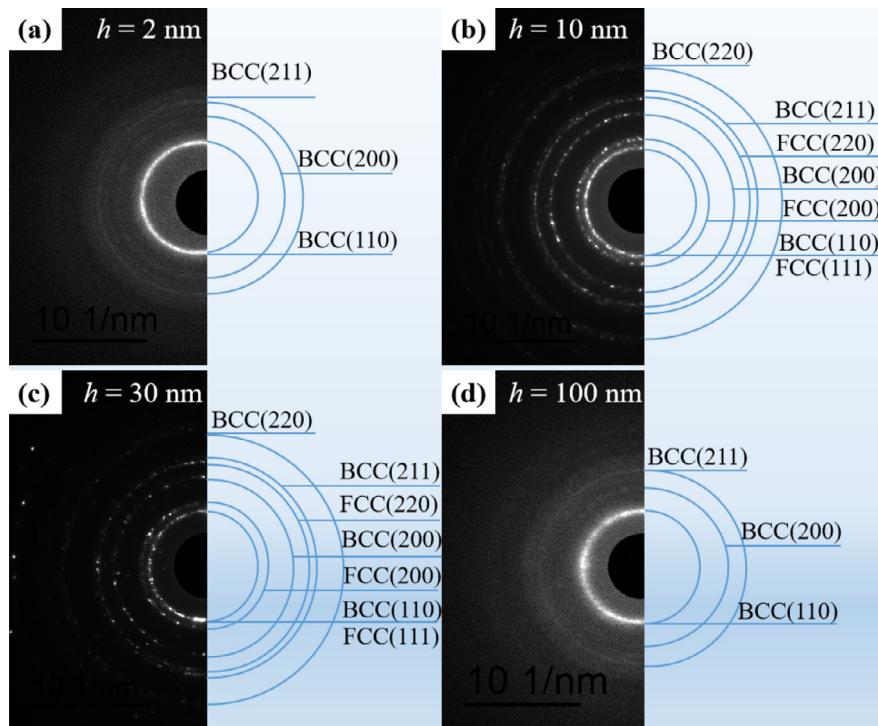


Fig. 5. The SAED patterns of irradiated Al_{1.5}CoCrFeNi HEA films with nominal individual-layer thickness (a) $h = 2\text{ nm}$, (b) $h = 10\text{ nm}$, (c) $h = 30\text{ nm}$ and (d) $h = 100\text{ nm}$.

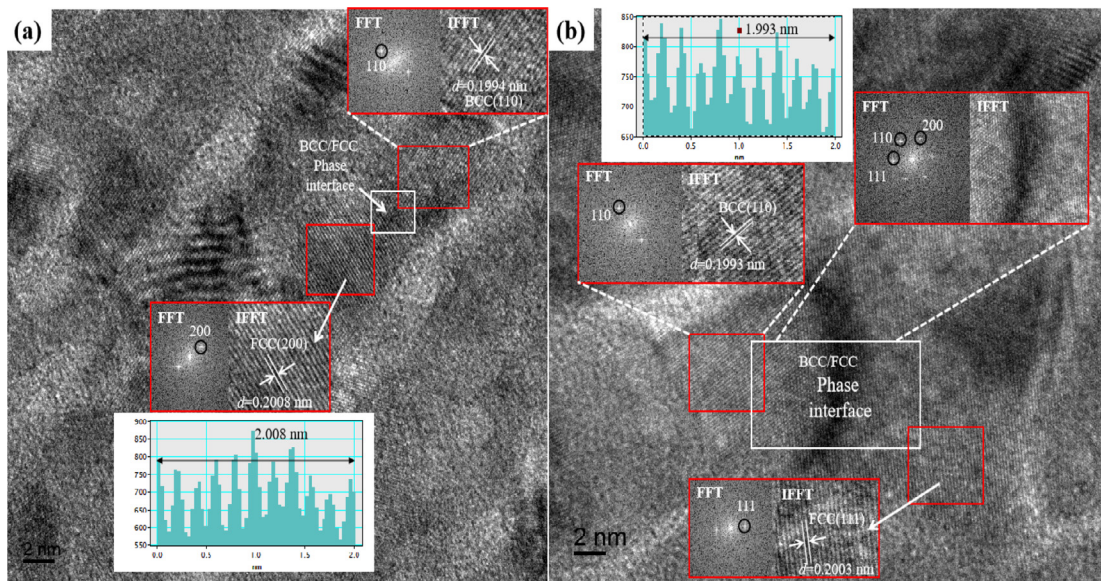


Fig. 6. The HRTEM images of multi-nanolayered HEA film with individual-thickness of (a) $h = 10\text{ nm}$ and (b) $h = 30\text{ nm}$, and the detailed phase structure obtained from FFT and IFFT images.

The representative composition maps of EDS for the irradiated HEA films of $h = 2$ and 30 nm are obtained from the damaged regions. As illustrated in the Fig. 8, a homogeneous composition distribution is revealed in the HEA film of $h = 2\text{ nm}$ without obvious enrichment and depletion of the alloy elements near the GB sinks. So the high-density GBs in the nano-crystalline HEA film ($h = 2\text{ nm}$) play an important effect in reducing the level of RIS by eliminating the point defects and facilitating the solute diffusion uniformity and interstitial/vacancy recombination, thus leading to the suppression of solutes enrichment and depletion at the defect sink, which is consistent with the limited RIS in the ultra-

fine grained 316 austenitic steel after heavy ion irradiation and in the nano-crystalline CoCrCuFeNi HEA after electron irradiation, respectively [36–37]. In contrary, the obvious element enrichment or depletion can be observed from the distribution maps of EDS in the sample of $h = 30\text{ nm}$. As shown in Fig. 9, the Al element serious enrichment (marked by red ellipses), Cr and Fe elements slight enrichment (marked by red ellipses), Co and Ni elements slight depletion (marked by white ellipses) are observed inside matrix, indicating that the instability of phase structure results from RIS of alloy elements under this irradiation damage level (the damage peak value is 7.01 dpa). These results are consistent with the RBS

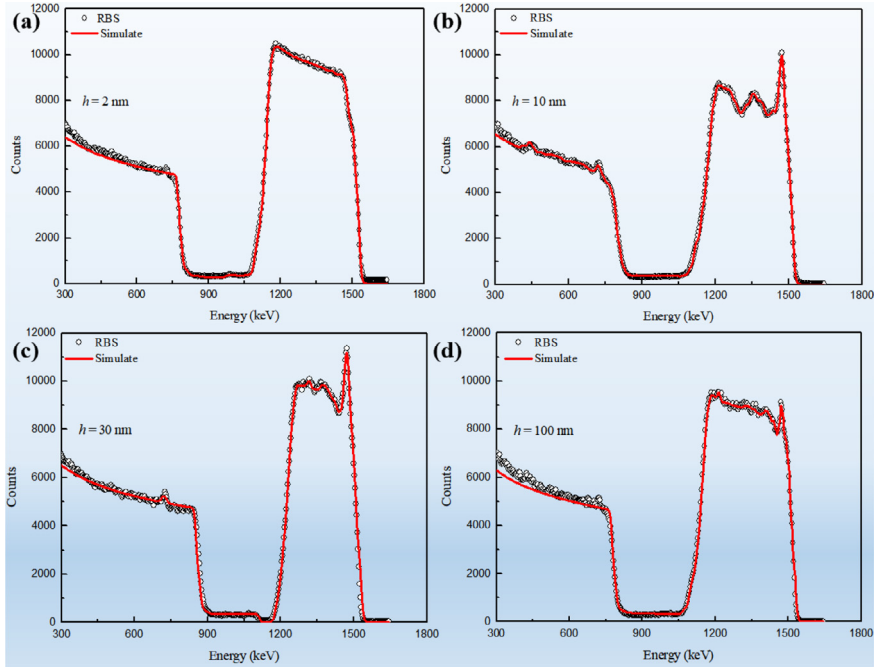


Fig. 7. RBS spectrum and simulated spectrum of irradiated $\text{Al}_{1.5}\text{CoCrFeNi}$ HEA film with (a) $h = 2 \text{ nm}$, (b) $h = 10 \text{ nm}$, (c) $h = 30 \text{ nm}$ and (d) $h = 100 \text{ nm}$, respectively.

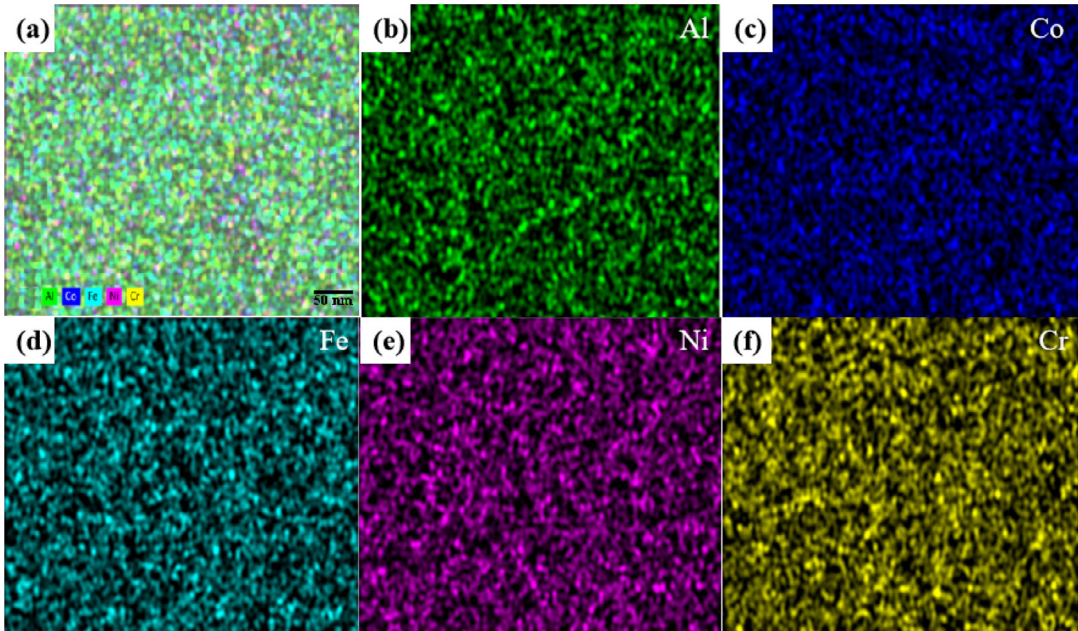


Fig. 8. The representative composition map of STEM-EDS were extracted from the irradiated $\text{Al}_{1.5}\text{CoCrFeNi}$ HEA film with $h = 2 \text{ nm}$ (a) Cross-sectional overlay map image and element maps (b) Al, (c) Co, (d) Fe, (e) Ni and (f) Cr, respectively.

spectra. Also, the irradiation-induced phenomena of Co, Ni depletion and Al, Fe, Cr enrichment at irradiated regions have been revealed in previous studies [14,19], causing a nonuniform distribution of alloy atom due to the irradiation-induced segregation. Similarly, the irradiation-induced partial BCC \rightarrow FCC phase transformation and element segregation were disclosed by low energy and high fluence He^+ induced vacancy-type defects in $\text{Al}_{1.5}\text{CrFeNi}$ films, and the remarkable diffusion and segregation of the alloy elements were elucidated in detailed [19]. Yang et al. [32] revealed that the FCC phase is enriched in Fe, Cr and Co, while the BCC phases are

enriched in Al and Ni due to the different negative formation enthalpy between the BCC and FCC structure.

3.5. Irradiation-induced swelling behavior

The height profile difference ΔH between the irradiated and masked regions (unirradiated) can be measured by AFM, as shown in Fig. S2, the measured values of ΔH are 3.0 nm, 6.2 nm, 7.9 nm and 3.6 nm for the HEA films of $h = 2 \text{ nm}$, 10 nm, 30 nm and 100 nm, respectively. The volume swellings and swelling rates of

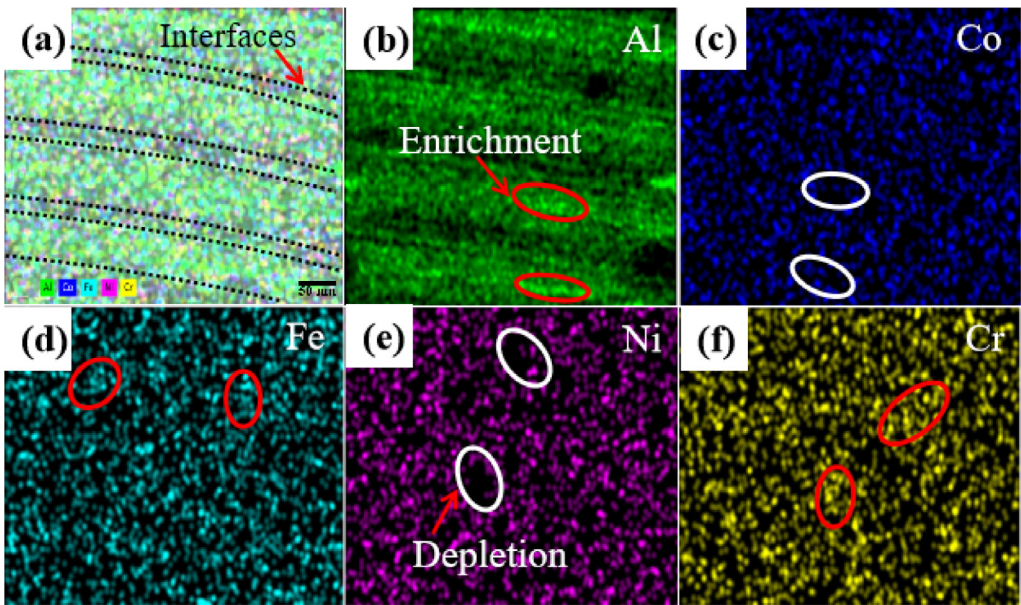


Fig. 9. The representative composition mapping of STEM-EDS were extracted from the irradiated $\text{Al}_{1.5}\text{CoCrFeNi}$ HEA film with $h = 30 \text{ nm}$ (a) Overlay map image and element maps (b) Al, (c) Co, (d) Fe, (e) Ni and (f) Cr, respectively.

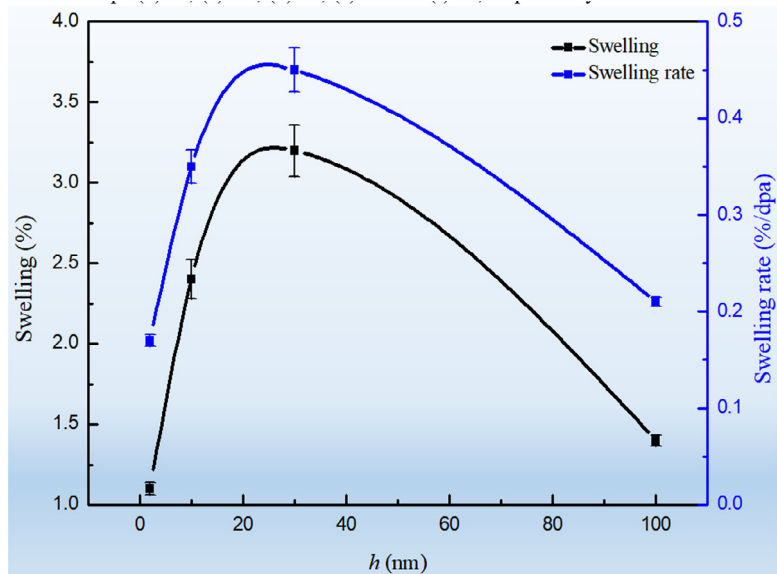


Fig. 10. The irradiation swelling and swelling rate of irradiated multi-nanolayered HEA films with h .

the multi-nanolayered HEA films irradiated to $1 \times 10^{17} \text{ cm}^{-2}$ were calculated following the ASTM standard E521-9615 using the equations [38]:

$$S(\%) = \frac{\Delta H}{L} \quad (3)$$

$$S_R(\%/\text{dpa}) = \frac{S\%}{DPA_{peak}} \quad (4)$$

where L is the depth of damaged region (about 250 nm) in these HEA films, DPA_{peak} is damage peak value of 7.01 obtained from Fig. S1. As shown in Fig. 10, the swellings and swelling rates in the HEA films with $h = 2$ and 100 nm are 1.1–1.4% and 0.7–0.21%/dpa within the damage peak region, which are significantly lower than the films with $h = 10$ and 30 nm (The swellings are 2.4–3.2%, swelling rates are 0.35–0.45%/dpa). These results indicate that the HEA films with $h = 2$ and 100 nm display lower swelling in comparison with

the HEA films with $h = 10$ and 30 nm due to the diverse sizes in bubbles and its primary distribution at GBs or interfaces.

3.6. Nano-hardness and elastic modulus

Fig. 11 presents the variation of the nano-hardness and elastic modulus with indentation depth in the as-deposited HEA films. As shown in Fig. 11(a) and (b), the slight variation of hardness with increasing indentation depth can be observed at the depth higher than 50 nm for as-deposited films, the behavior of depth dependent nano-mechanical properties has been investigated as an indentation size effect (ISE) [39]. Conversely, within the depth less than 50 nm, the nano-mechanical properties display drastic vibration with the indentation depth due to the surface roughness, which was recognized as reverse ISE [39]. A soft substrate effect may be produced as the underlying depth higher than 250 nm in matrix. In the depth of 50–

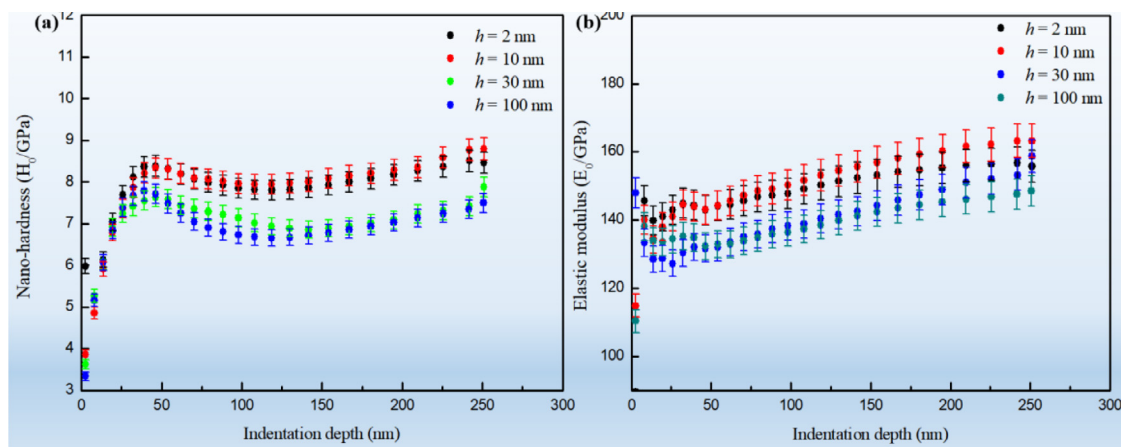


Fig. 11. Indentation depth dependence of the (a) nanoindentation hardness and (b) the elastic modulus for as-deposited HEA films with nominal monolayer thickness h , respectively.

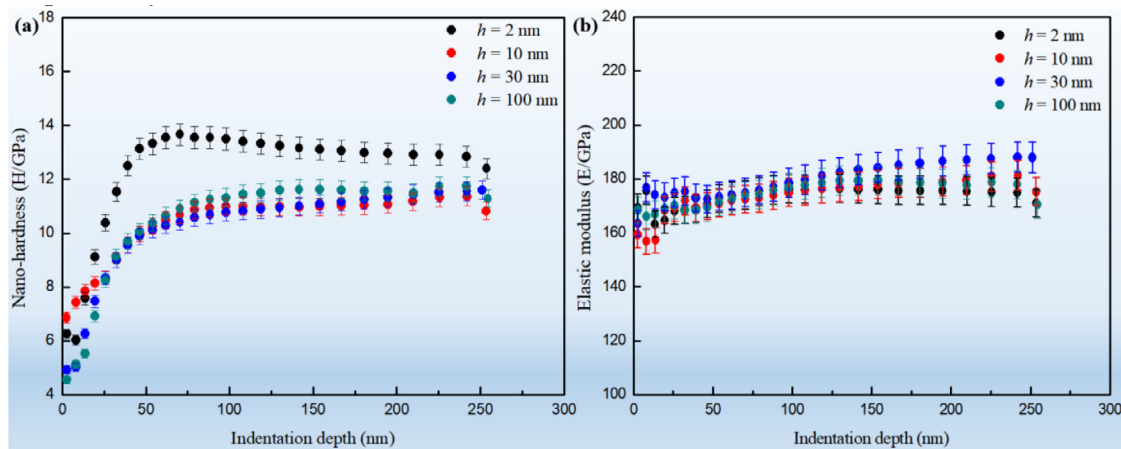


Fig. 12. Indentation depth dependence of the (a) nanoindentation hardness and (b) the elastic modulus for irradiated HEA films with nominal monolayer thickness h , respectively.

250 nm, the nano-mechanical properties exhibit slight increase tendency, indicating that the nano-GBs and interfaces are beneficial to the improvement of mechanical behavior. Both the nano-hardness and elastic modulus present basically identical variation in the films of $h = 2$ and 10 nm. Then, the nano-hardness and elastic modulus decrease in the films of $h = 30$ and 100 nm due to the reduction of interface numbers, this may explain the relative sensitivity of the nano-mechanical properties to interfacial effects.

Fig. 12 shows the the nano-hardness and elastic modulus with indentation depth for the irradiated HEA films. Here the “Depth-hardness” and “Depth-elastic modulus” curves have different tendencies with the indentation depth, which is correspond to variation of nano-mechanical properties in response to the irradiation-induced damage in the irradiated HEA films. On the one hand, the nano-hardness in irradiated samples show increase trend compared with the as-deposited films due to irradiation-induced hardening behavior. On the other hand, the values of nano-hardness in the HEA films with $h = 2$ and 100 nm are obviously higher than the HEA films with $h = 10$ and 30 nm. At the same time, the elastic modulus first decrease and then increase with h in the HEA films. The variation of mechanical properties is closely associated with the different He behavior, defects and phase-structure evolution in these films.

Fig. 13(a) displays the hardness and elastic modulus with error bars as a function of nominal monolayer thickness h , in which the data are the average values between 50 and 250 nm chosen from the “Depth-hardness” and “Depth-elastic modulus” curves of the irradiated films. When the monolayer thickness is adjusted from 2 nm to 10 nm, the nano-hardness and elastic modulus are both decreased from 13.19 ± 0.39 GPa and 175.01 ± 1.75 GPa to 10.94 ± 0.33 GPa and 176.30 ± 1.76 GPa, respectively. Then, the nano-hardness and elastic modulus are enhanced slightly to 11.36 ± 0.34 GPa and 176.67 ± 1.77 GPa when the h is increased from 10 to 100 nm. The relative hardening rate H/H_0 (H : irradiated hardness, H_0 : unirradiated hardness) of the HEA films as a function of indentation depth is shown in Fig. 13(b). The values of H/H_0 display enhanced tendency within the irradiation damage depth of 150 nm, while the H/H_0 slightly decrease in the depth of serious damage-regions (150–250 nm) due to the higher defect-density. The higher H/H_0 in irradiated HEA films of $h = 2$ nm and 100 nm can be explained by the dispersed distribution of bubbles and irradiation-induced dislocations, which effectively hinder the dislocation mobile to increase relative hardening rate. It is worthy of noting that the maximum H/H_0 is demonstrated at the damage peak region for the HEA film of $h = 100$ nm, suggesting that the distributed He bubbles at GBs and limited interfaces enhance the relative hardening rate synergistically. Besides, the large-sized bub-

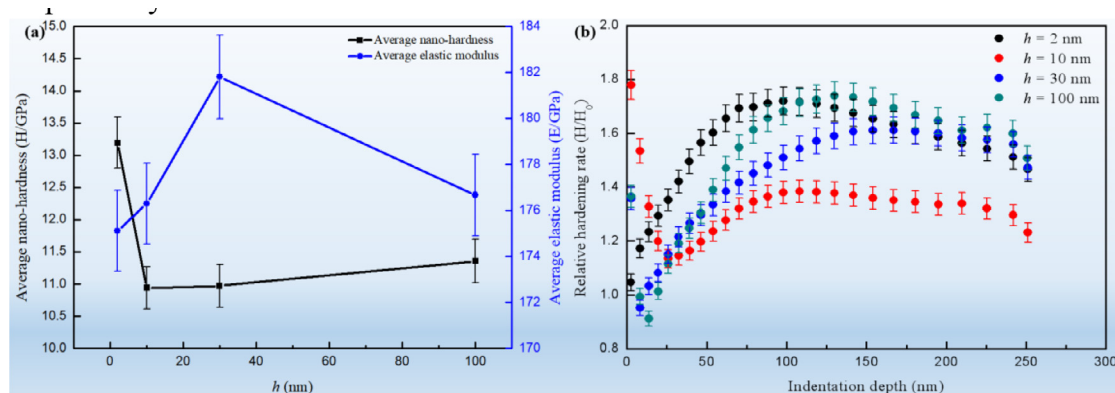


Fig. 13. (a) The averaged nanoindentation hardness and elastic modulus for HEA films with nominal monolayer thickness h ; (b) variation of relative hardness H/H_0 (H : irradiated hardness, H_0 : unirradiated hardness) as a function of indentation depth.

bles and the formation of FCC phase are responsible for the lower relative hardening rate for the HEA films of $h = 10$ and 30 nm. The detailed hardening mechanism will be explained in the following discussion part.

4. Discussion

4.1. Influences of interfaces on He behavior

The experimental results show that He evolution exhibits two different behavior in the various HEA films. He bubbles are formed in the films without abundant interfaces for the generation of a mature bubble (namely in the films with $h = 2, 100$ nm). While bubbles with average sizes of 3–4 nm are formed in the multi-nanolayered HEA films ($h = 10, 30$ nm) with a large number of interfaces. The energetic He^+ will trigger cascade collisions and cause a massive displacement, which generates a number of point defects, including interstitials and vacancies, which can assist He diffusion and migration as medium [40]. He atoms injected into the crystalline lattice of HEA films during irradiation migrate via jumps between interstitial positions before trapping with vacancies [41]. Previous calculation has shown that the formation energies of He defects are substantially reduced in the cores of GB dislocations [42], particularly at the GB intersections, which act as effective defect sinks to trap He in the HEA film ($h = 2$ nm) with high-density GBs, which can prompt He bubble growth with ribbon-like structure along the GB intersections and reduce the rate of He accumulation within the grains themselves [21–23]. The sluggish diffusion effect [43] in HEA film can explain the formation of smaller-sized bubbles. The GB is regarded as dominant mechanism for He atoms migration in the intersections to agglomerate He bubbles and then effectively annihilate the irradiation-induced defects (interstitials and vacancies) in grains, which is also confirmed by the computational simulation [44].

Because of the unambiguous multi-nanolayered interfaces in HEA films of $h = 10$ and 30 nm (Fig. 2(b) and (c)), the diffusion and mobility of small-sized bubbles or He atoms are enhanced through the nano-GBs, facilitating the bubble growth and distribution with ribbon-like structure throughout the interfaces. Theoretically, the process of bubble formation can be divided into three stages [41] (or four stages including the incubation): nucleation by clustering of He atoms, growth by absorption of mobile He atoms, and coarsening by migration of the smaller bubbles. The increased interfaces play a dominate role in the formation of He bubbles at interfaces compared with the HEA film of $h = 2$ nm. In view of the atomic-level, the interfaces in multi-nanolayered $\text{Al}_{1.5}\text{CoCrFeNi}$

HEA films ($h = 10, 30$ nm) with lattice mismatch/distortion or various element compositions have vast misfit vacancies and interstitials, which are regarded as the preferred sites for He trapping and nucleation of He cluster or bubble [45]. A schematic diagram describes the influence of the defect-interface interaction, which is shown in Fig. 14(a). Here, a combination of He atoms and vacancy-type defects precipitates into relatively flat platelets, rather than spherical He bubbles due to the interfaces with a non-uniform, location-dependent interface energy [45]. In particular, the local interface energy is so high that there is a thermodynamic driving force for precipitated He platelets, which is composed of nanometer He-vacancy complexes. He platelets contact with the interface and further expand into the surrounding lower-energy regions with increasing of He trapping [45,46]. The existing results indicated that the contact area of bubbles with interface remains unchanged owing to the Cu lamellae with lower surface energy, the bubbles prefer to migrate into the Cu layer in the Cu/Nb multi-nanolayered films, suppressing bubble growth at interface and damaging the Cu lattice [44–47]. However, the multi-nanolayered $\text{Al}_{1.5}\text{CoCrFeNi}$ HEA films are taken as a similar structure regardless of the composition difference, the homogeneous interface is contributed to the improved ability of store He and diverse He morphology. With increasing of interface numbers, the GB intersections are reduced significantly, especially for the sample of $h = 10$ nm, resulting in the He diffusion and migration into interfaces through GBs and the formation of He platelets at initial stage. Above a critical He concentration at the surrounding of He platelet sites, the He platelet transforms into spherical bubble during irradiation. Kashinath et al. [45–47] pointed out that the He morphology transition from platelet to bubble was driven by a competition between three kinds of pressure acting on He-filled cavities (accumulation with several He platelets) at interfaces: the mechanical pressure P_{He} of the trapped He atoms, the osmotic pressure P_V due to the flux of radiation-induced vacancies within the crystal to the cavity, and the capillary pressure P_C arising from the surface energy of the cavity. P_{He} and P_V tend to expand the cavity while P_C tends to shrink it. When these three pressures balance, i.e.,

$$P_{\text{He}} + P_V = P_C \quad (5)$$

then the cavity is in equilibrium; that is, it neither expands nor contracts. For the multi-nanolayered HEA films ($h = 10, 30$ nm), P_{He} and P_V continuously increase with increasing He concentration at platelet sites, leading to the occurrence of platelet-to-bubble transitions. The transited bubble further expands into both sides of HEA film-layers and the interface planer maintains the spher-

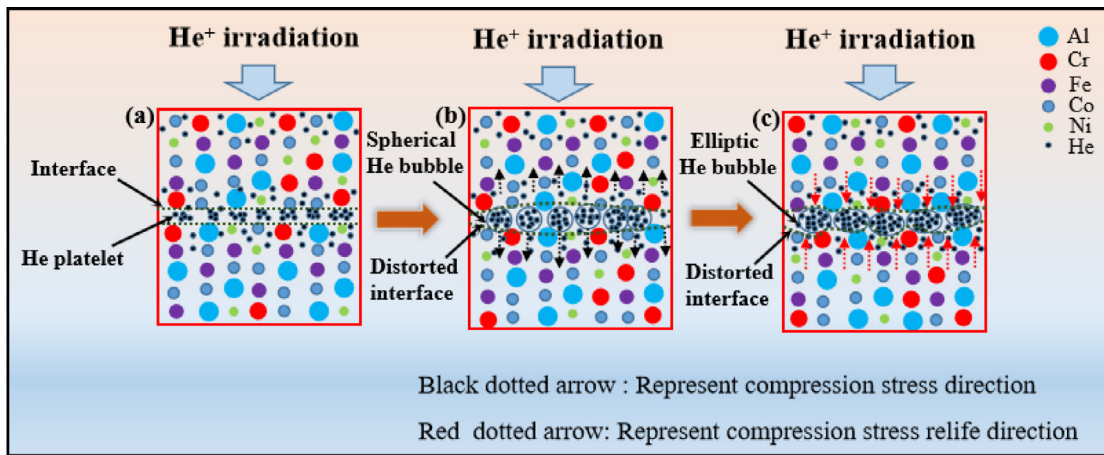


Fig. 14. Schematic illustration of the He morphology evolution for the multi-nanolayered $\text{Al}_{1.5}\text{CoCrFeNi}$ HEA films with $h = 10$ or $h = 30$ nm which irradiated at fluence of $1 \times 10^{17} \text{ cm}^{-2}$. (a) He platelet formation by He trapping effects at interface; (b) Spherical He bubble formation at interface; (c) Elliptic He bubble formation at interface.

ical bubble stability during the platelet-to-bubble transitions. The corresponding schematic diagram is illustrated in Fig. 14(b). The lattice distortion and shrinkage induced by high strain energy in the HEA film layer suppress He bubble further expanding into both sides of film layer. The spherical He bubble is pressed by the release of compression stress coming from film layer, which is contributed to bubbles expanding into interface planer by increasing its contact area with the interface, the ribbon-like bubbles are formed through interconnection of elliptic bubbles along the multi-nanolayered interface, as shown in HRTEM characterization results and the graphical presentation in Fig. 14(c).

Besides, the period of bubble growth is closely related to the coarsening by the small-sized bubbles. Bubble coarsening process in multi-nanolayered $\text{Al}_{1.5}\text{CoCrFeNi}$ HEA films ($h = 10, 30$ nm) can be interpreted by below two different mechanisms [48]: (1) Ostwald ripening (OR), which signify that large bubbles enhance its volume at the expense of adjacent isolate and smaller bubbles or individual He atoms, which diffuse through the matrix lattice before being captured [49]; and (2) Bubble migration and coalescence, which means small He bubbles move through the lattice via thermal movement and surface diffusion, and grow by coalescing with each other [50]. The pressure inside He bubble depends on the conditions and the stage of the bubble evolution, i.e., irradiation temperature, He production and displacement rates, He concentration and fluence, as well as bubble size. It is well known that, at room temperature, the state of He is either fluid or solid depending on the pressure. The state equation of He bubble is used to approximately quantify the bubble pressure (P), as given by the following equation [51]:

$$P = 2\gamma_{SV}/r + \sigma \quad (6)$$

where γ_{SV} is the surface free energy, r is the bubble radius, and σ is the stress around the bubble. The surface energy γ_{SV} for the $\text{Al}_{1.5}\text{CoCrFeNi}$ HEA is estimated to be about $1.8103 \text{ J}\cdot\text{m}^{-2}$, which was calculated by averaging the surface energy of each element [52]. Under equilibrium conditions for these HEA films, where $\sigma = 0$, $P = 0.9\text{-}1.8 \text{ GPa}$. Under the condition of dislocation punching, $\sigma \approx \mu b/r$, $\mu \approx 108 \text{ GPa}$, $b = 0.25 \text{ nm}$, $P = 15.3\text{-}30.6 \text{ GPa}$. Thus, the interior pressures are $0.9\text{-}30.6 \text{ GPa}$ inside bubbles with diameters of $2\text{-}4 \text{ nm}$ in these HEA films.

Further reducing the interface numbers ($h = 100 \text{ nm}$), the numbers of GB intersections are increased, which enhances the probability of He atoms trapped by the GB when these He atoms are migrating into the matrix. The enhanced GB intersections reduce the He concentration for the generation of a mature bubble. Based on the He evolution process of platelet-to-bubble transitions, the

formed He platelets have higher capillary pressures than bubbles owing to the higher surface-to-volume ratios in the relatively flat He platelets [45,21]. The higher capillary pressure is able to balance the mechanical and osmotic pressures that tend to expand the small He cluster into platelet structure at the interface, stabilizing it against growth into large-sized bubbles. Dispersed bubbles are mainly distributed at GB intersections because of the limited interface numbers. The diffusion distance is dramatically increased for the abundant He interstitials or vacancy defects to diffusion from the original location to nearest interface sinks. K.Y. Tsai et al. [43] revealed that the high activation energy and low atomic diffusion mobility result from the significant atomic traps and blocks in CoCrFeMnNi HEA due to the greater fluctuation of lattice potential energy. Although there is a distinct difference between solute atomic diffusion and He interstitial diffusion on account of its very low solubility and ability of forming bubbles, the sluggish diffusion effect and high activation energy can also provide a mechanism for explaining the suppression of bubble growth in the multi-nanolayered film of $h = 100 \text{ nm}$.

4.2. Phase transformation and RIS mechanism in multi-nanolayered HEA films

Except for the He evolution behavior, the phase transformation resulted from RIS behavior also exhibits different tendency with the size of h . In general, previous extensive RIS investigation has been done on the conventional alloys with one or two principal elements. It is certificated that RIS behavior is an enhanced diffusion of components of alloys in irradiation regions under the effect of rapidly migratory and aggregation of point defects (vacancies and interstitials), leading to enrichment or depletion of alloy elements near defect sinks (such as, high angle grain boundaries, dislocation loops and voids, etc) in the irradiated materials [53,54]. It is interesting to note that the phase stability in HEA films with $h = 2, 100 \text{ nm}$, the injected He^+ are preferentially trapped by vacancies to form He bubbles at GBs, dispersing He aggregation and suppressing the migration and growth of bubble. At the same time, the dispersed He bubbles degrade stress concentration and reduce composition enrichment or depletion. High stress field will be generated near the defects sinks with increasing the irradiation damage, phase transformation and RIS behavior are generally associated with relief of high internal stress levels and plastic deformation [55]. The lattice distortion and shrinkage are induced by residual compression-stress during platelet-to-bubble transitions and the bubble growth in the multi-nanolayered HEA films with $h = 10$ and 30 nm , as disclosed in GIXRD patterns and

HRTEM analysis. Thus, the partial BCC→FCC phase transformation and compositional reorganization are prompted by the relief of compression stress in each film layer, the relief direction of stress is shown in the schematic illustration of Fig. 14(c). Xu et al. [56] revealed irradiation-induced BCC phase formation in austenitic stainless steel due to the stress relief caused by Xe gas bubbles and stacking faults formation. The precipitate of the second phase and RIS behavior mitigate the lattice strain or lattice distortion of the solid-solution matrix to a certain extent [57]. Therefore, the lattice stress relief and compositional changes in matrix are the driving forces for FCC-phase formation in multi-nanolayered HEA films of $h = 10$ nm and 30 nm during He^+ irradiation.

The phase transformation and RIS behavior are also closely associated with the diffusion kinetics of solute atoms, which generally can be explained by the two diffusion and migration models: (1) Interstitial-solute binding mechanism and (2) Inverse Kirkendall Effect (IKE) mechanism. The interstitial-solute binding model was proposed by Okamoto and Wiedersich [58], which means that the undersized solutes can tightly bind to interstitials forming interstitial-solute complexes that migrate as solute interstitials. As a result, the undersized solutes were transported to the defect sinks by in-place rotation and exchanged with the configurations of mixed interstitial-solute. If the RIS in irradiated multi-nanolayered $\text{Al}_{1.5}\text{CoCrFeNi}$ HEA films ($h = 10, 30$ nm) is controlled by the interstitial-solute bonding mechanism, the undersized solute Ni and Co coupling with other interstitials (Fe or Cr atoms) would be enriched near interface sinks based on this diffusion model (The atom radius is summarized as follows: $R_{\text{Al}} > R_{\text{Cr}} > R_{\text{Fe}} > R_{\text{Co}} > R_{\text{Ni}}$). It is not in agreement with the Fe and Cr depletion in the irradiated multi-nanolayered film of $h = 30$ nm. Wiedersich and Lam et al. [59] considered that the interstitial-solute bonding mechanism generally was used to describe the diffusion in dilute alloy rather than in concentrated solid solution alloy, such as high entropy alloy or multi-principal element alloy.

For comparing general understanding in RIS between conventional and compositionally complex HEAs, the RIS behavior in the irradiated multi-nanolayered HEA film ($h = 30$ nm) can be explained by the vacancy-dominated IKE mechanism [18,19,60,61], which means the solute enrichment and depletion by a coupling between the defect fluxes and fluxes of alloying elements. It is well known that high-density GBs can attract both interstitials and vacancies, efficient reducing vacancy concentration in the grains by the combination of He and vacancy to form bubbles in the films of $h = 2, 100$ nm, which is contributed to the suppression of defect flux toward the defect sink and subsequent weak RIS behavior according to the mechanism of IKE [61,62]. However, the significant RIS behavior occurred in the film of $h = 30$ nm due to the fact that interface is considered as free surface, which offers enough vacancy flux for the solute diffusion each other. Meanwhile, RIS has been recognized that equilibrium segregation of certain alloying elements to external surfaces occur as a consequence of the concurrent reduction of the surface free energy, a similar segregation phenomenon occurs at the external irradiated surface in nickel-ion bombarded 18Cr-8Ni-1Si stainless steel [63]. It was particularly noteworthy that the undersized solute atom was a slow diffuser and the oversized solute atom was a rapid diffuser due to the effect of bonding characteristics of the d electrons [64]. Johnson and Lam [65] also found the diffusivities following the order $D_{\text{Cr}} > D_{\text{Fe}} > D_{\text{Co}} > D_{\text{Ni}}$ in CoCrFeNi multi-principal element alloy by using the radiotracer method. The Al atom has much lower activation energy of self-diffusion ($142.0 \text{ kJ}\cdot\text{mol}^{-1}$) and thus decreases the average level of activation energy of diffusion in the lattice of the present alloy system [66]. The IKE mechanism in concentrated solid solution alloys is illustrated schematically in Fig. 15(a) [67], the oversized A atoms diffuse faster than undersized B atoms, hence the flux of vacancies toward the defect sink induces a preferential flux

of A atoms in the opposite direction. The fluxes of vacancies and atoms satisfy the following relationship [67]:

$$-J_V = J_{AV} + J_{BV} \quad (7)$$

J_V is total vacancy flux, J_{AV} and J_{BV} represent the flux of oversized A atoms and undersized B atoms, respectively. The diffusion of vacancy and solute atom by exchange inside the lattice are illustrated in Fig. 15(b), the flux of vacancy toward the defect sink induces a preferential flux of oversized atoms Al, Cr and Fe in the opposite direction. The Al, Cr and Fe atoms become depleted at defect sink of interface due to its faster diffusion while the defect sink of interface becomes enriched in Co and Ni atoms with slower diffusion. According to the above analysis, the phase transformation and RIS behavior in the multi-nanolayered HEA films ($h = 10, 30$ nm) are determined synergistically by lattice relief of compression stress and the interaction of the vacancy-type defects and solute atoms, moreover, the migration behavior of RIS depends on the different diffusivities for various atomic size of the alloy elements.

4.3. Effects of interface on the radiation-induced swelling behavior

Hayns and Williams et al. [68] proposed that low swellings are due to the reductions in vacancy supersaturation by enhanced mutual He-vacancy recombination, which results from He atoms trapping at GBs preferentially. The nano-GBs in the HEA films of $h = 2$ and 100 nm play dominated role in improving swelling resistance by reducing the size of He bubbles, which is consistent with the previous research reports that the grain boundaries act as strong point defect sinks and suppress swelling by reducing the vacancy [69]. The irradiation-induced vacancies are easily occupied by He atoms to form smaller-sized bubbles, which are further diffused into GBs, reducing the He accumulation and swelling. On the contrary, ribbon-like He bubbles in films ($h = 10, 30$ nm) are accumulated at interfaces during irradiation, resulting in more significant swelling and swelling rate than the HEA films with $h = 2, 100$ nm. The relative change of unit cell volume ($\Delta V/V$) (as shown in Table 1) presents negative value in the films with $h = 10, 30$ nm, this result can only indicate the lattice shrinkage in each film layer from the mechanical pressure of He bubble. While the volume swelling of multi-nanolayered HEA films ($h = 10, 30$ nm) is induced by the expansion of bubble volume at interface or inside film matrix.

4.4. Effects of interface on the radiation-induced mechanical properties evolution

Compared with the as-deposited HEA films, the higher hardness and elastic modulus take place in the irradiated HEA films with various h . The variations of H/H_0 also exhibit evident enhancement in the HEA films with $h = 2$ and 100 nm in contrast with the films of $h = 10$ and 30 nm. The enhancements in hardness for these films of $h = 2$ and 100 nm are considered mainly resulting from the radiation induced smaller-sized bubbles. Based on a dispersed barrier hardening model [70], the increase in yield stress $\Delta\sigma_y$ is equal to the increase in applied stress required to move a dislocation line through a field of obstacles:

$$\Delta\sigma_y = \frac{1}{8}M\mu bdN^{2/3} \quad (8)$$

where M is Taylor factor of 3.06 (for equiaxed BCC and FCC polycrystals), μ is shear modulus about 108 GPa and b is the Burgers vector of the primary glide dislocations, where N and d is the average bubble density and bubble diameter, respectively. Average He bubble density is about $3.6 \times 10^{22} \text{ m}^{-3}$ and the average bubble diameter is 1.5 nm in the film of $h = 2$ nm which is calculated

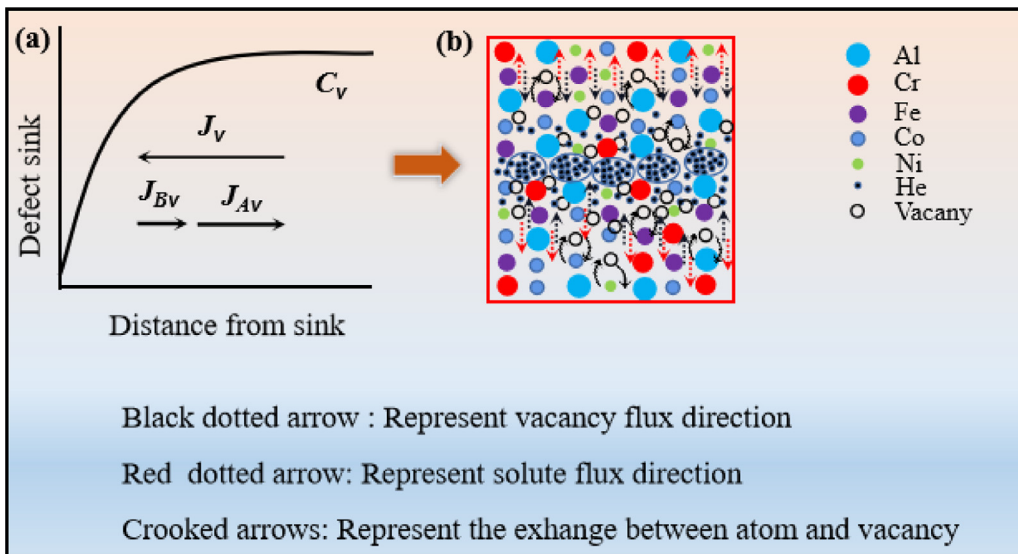


Fig. 15. Schematic illustration of the RIS behavior for the multi-nanolayered Al_{1.5}CoCrFeNi HEA films of $h = 10$ or $h = 30$ nm. (a) Illustration of the fluxes of vacancies and atoms in the inverse Kirkendall effect [67]; (b) Illustration of the diffusion of vacancy and solute atom by exchange inside the lattice, as well as the solute and vacancy flux direction.

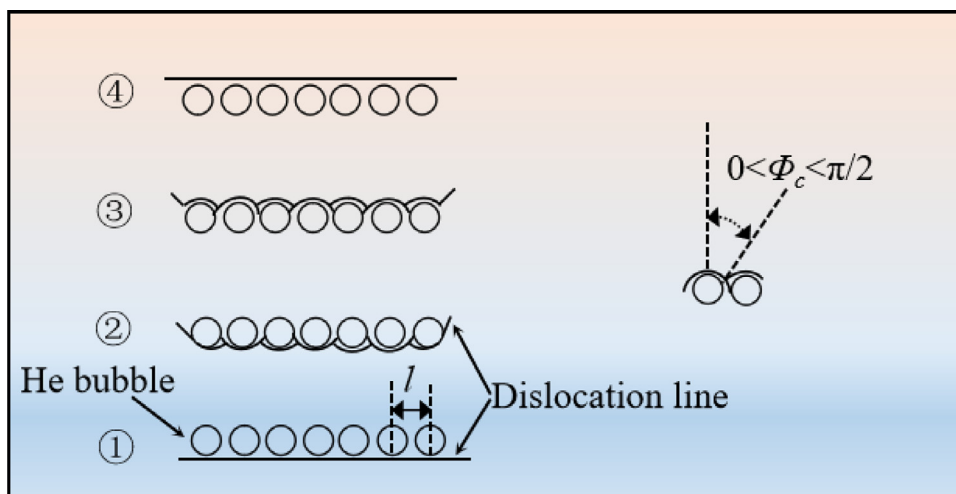


Fig. 16. Schematic illustration of glide dislocation interaction with nano-scale bubbles of spacing l . Numbers ①–④ show the steps of dislocation line movement through a field of bubbles. Φ_c is the semi-critical angle at which the dislocation breaks away from He bubbles.

approximately from the damage regions. While the bubble density and bubble diameter are significantly increased to about $1.4 \times 10^{22} \text{ m}^{-3}$ and 2.5 nm in the film of $h = 100$ nm because of the trapping effect of He atoms at GBs (shown in Fig. 3(d)). The calculated $\Delta\sigma_y$ in the film of $h = 2$ nm is larger than the film of $h = 10$ nm, which proves that the high-density He bubbles and dislocations are responsible for the improved hardness. However, the sharply reductions of hardness and H/H_0 in $h = 10, 30$ nm are attributed to the bubble formation through large-sized bubble accumulation and growth in comparison with the HEA films of $h = 2, 100$ nm.

Compared with the as-deposited HEA films with $h = 10, 30$ nm, the formed He bubbles at multi-nanolayered interfaces can enhance the nano-hardness, elastic modulus and H/H_0 , which is well consistent with the Ag/V multi-nanolayered films after He⁺ irradiation [71,72]. The weak obstacles, such as large-sized bubbles, are responsible for the lower mechanical properties. Bubbles size and density will greatly influence the hardening effects [73,74]. The interaction mechanism between the bubbles and interfaces was used to describe He bubble hardening behavior in multi-nanolayered

HEA films, as shown schematically in Fig. 16. The weak obstacles (He bubbles) can overcome the applied shear stresses which less than that needed to bend the dislocation line to a semicircle. The shear stress τ needed to move a dislocation past two penetrable obstacles with a distance l , and thus the modified Orowan equation as follows [75]:

$$\tau = \frac{\mu b}{2\pi l} \ln\left(\frac{1}{d}\right) (\cos \varphi_c)^{1/2} \quad (9)$$

where Φ_c is half of the critical bow-out angle between dislocation lines cutting through the obstacles. For the weak obstacles, the $0 < \Phi_c < \pi/2$ [72]. The dislocation can bypass through the bubble and interface according to the modified Orowan model. Weak hardening rate is found for the films with $h = 10$ and 30 nm, this implies that interface He bubbles effectively boost dislocations line glide, so the He bubbles at interfaces result in a modest hardening increment in nano-multilayered films as compared to He bubbles in the films ($h = 2, 100$ nm) with high-density nano-GBs. The He bubbles at interfaces also triggered crystalline embrittle-

ment, which may treat as another mechanism in the deterioration of hardening effect for the multi-nanolayered HEA films. Meanwhile, the formation of FCC phase in the multi-nanolayered films of $h = 10$ nm and 30 nm also leads to the reduced hardening behavior due to the FCC phase with lower mechanical properties in the $\text{Al}_x\text{CoCrFeNi}$ system ($x = 0\text{-}3$) [76].

5. Conclusion

In summary, the dependence of micro-structure, irradiation swelling and mechanical properties on the tunable thickness size h in multi-nanolayered $\text{Al}_{1.5}\text{CoCrFeNi}$ HEA films with high-density GBs and homogeneous interfaces were investigated systematically in this study. The results revealed that the smaller-sized bubbles (1-2 nm) preferentially distributed along the GB intersections and the phase structure kept stability in the irradiated $\text{Al}_{1.5}\text{CoCrFeNi}$ HEA films with $h = 2$ and 100 nm since the high-density GB intersections acted as dominated reason to trap He atoms. The dispersed distribution of GB was responsible for the reduced He accumulation within the grains themselves and improved phase stability by reducing vacancy concentration. While the reverse phenomenon that the distribution of He bubbles throughout the interfaces and the partial BCC \rightarrow FCC phase transformation due to RIS behavior were both disclosed due to the introduction of high-density interfaces in the irradiated multi-nanolayered HEA films ($h = 10$ and 30 nm). The intrinsic mechanism of bubble formation has been also discussed based on the He behavior in the multi-nanolayered HEA films with coexistence of nano-crystal and homogeneous interface. The underlying mechanisms of phase transformation and RIS were also interpreted by the relief of compression stress in lattice and vacancy-flux induced segregation behavior which depends on the different diffusivities for various atomic-size of the alloy elements. Moreover, the role of GBs/interfaces and irradiation defects on irradiation swelling and mechanical properties as well as corresponding mechanisms in the various-structure HEA films were also discussed in detail.

Declaration of Competing Interest

The authors declare that they have no known competing financial interests or personal relationships that could have appeared to influence the work reported in this paper.

CRediT authorship contribution statement

Guo Pu: Conceptualization, Methodology, Investigation, Formal analysis, Writing – original draft, Writing – review & editing. **Liwei Lin:** Software, Formal analysis, Funding acquisition. **Ding Ren:** Conceptualization, Supervision. **Kefu Gan:** Investigation, Visualization. **Bin Liu:** Methodology, Investigation. **Zongbiao Ye:** Writing – review & editing. **Yihan Wang:** Writing – review & editing, Supervision. **Kun Zhang:** Methodology, Investigation, Writing – review & editing. **Zhiming Li:** Writing – review & editing. **Bo Liu:** Methodology, Resources, Writing – original draft, Writing – review & editing, Supervision, Funding acquisition.

Acknowledgments

This work was supported by NSAF (Grant No. U2130115), the Sichuan Science and Technology Program (Grant NO: 2022YFSY0020) and the National Key Research and Development Program of China (Grant 2018YFA0702100). The author Kun Zhang is grateful to the Fundamental Research Funds for the central Universities for its financial supports.

Supplementary materials

Supplementary material associated with this article can be found, in the online version, at doi:[10.1016/j.jnucmat.2022.153734](https://doi.org/10.1016/j.jnucmat.2022.153734).

References

- [1] S.J. Zinkle, G. Was, Materials challenges in nuclear energy, *Acta Mater.* 61 (2013) 735–758.
- [2] J.W. Yeh, S.K. Chen, S.J. Lin, J.Y. Gan, Nanostructured high-entropy alloys with multiple principal elements: novel alloy design concepts and outcomes, *Adv. Eng. Mater.* 6 (2004) 299–303.
- [3] M.C. Troparevsky, J.R. Morris, M. Daene, Beyond atomic size and hume-rolles: understanding and predicting high entropy alloys, *JOM* 67 (2015) 2350–2363.
- [4] B. Gludovatz, A. Hohenwarter, D. Catoor, E.H. Chang, A fracture resistant high entropy alloy for cryogenic application, *Science* 345 (2014) 1153–1158.
- [5] H. Jiang, D.X. Qiao, W.N. Jiao, K.M. Han, Y.P. Lu, P.K. Liaw, Tensile deformation behavior and mechanical properties of a bulk cast $\text{Al}_{0.9}\text{CoFeNi}_2$ eutectic high-entropy alloy, *J. Mater. Sci. Technol.* 61 (2021) 119–124.
- [6] S. Chang, K.K. Tseng, T.Y. Yang, D.S. Chao, J.W. Yeh, Irradiation-induced swelling and hardening in HfNbTaTiZr refractory high-entropy alloy, *Mater. Lett.* 272 (2020) 127832.
- [7] Z.J. Zhang, E.H. Han, C. Xiang, Irradiation behaviors of two novel single-phase bcc-structure high-entropy alloys for accident-tolerant fuel cladding, *J. Mater. Sci. Technol.* 84 (2021) 230–238.
- [8] S.J. Zhao, Defect properties in a VtaCrW equiatomic high entropy alloy (HEA) with the body centered cubic (bcc) structure, *J. Mater. Sci. Technol.* 44 (2020) 133–139.
- [9] X.L. Ren, W.W. Zhang, B.D. Yao, J.Y. Zhang, Y.X. Wang, The prediction of untraceable solute behaviors of helium in high-entropy alloys, *J. Nucl. Mater.* 547 (2021) 152820.
- [10] Y.P. Lin, T.F. Yang, L. Lang, H.Q. Deng, C. Shan, W.Y. Hua, F. Gao, Enhanced radiation tolerance of the Ni-Co-Cr-Fe high-entropy alloy as revealed from primary damage, *Acta Mater.* 196 (2020) 133–143.
- [11] P.D. Edmondson, C.M. Parish, Y. Zhang, A. Hallén, M.K. Miller, Helium entrapment in a nanostructured ferritic alloy, *Scr. Mater.* 65 (2011) 731–734.
- [12] M.S. Staltssov, I.I. Chernov, B.A. Kalin, Peculiarities of helium bubble formation and helium behavior in vanadium alloys of different chemical composition, *J. Nucl. Mater.* 461 (2015) 56–60.
- [13] R.W. Harrison, G. Greaves, H. Le, H. Bei, Y. Zhang, S.E. Donnelly, Chemical effects on He bubble superlattice formation in high entropy alloys, *Curr. Opin. Solid State Mater. Sci.* 23 (2019) 100726.
- [14] W.T. Lin, G.M. Yeli, G. Wang, J.H. Lin, S.J. Zhao, D. Chen, S.F. Liu, F.L. Meng, Y.R. Li, F. He, Y. Lu, J.J. Kai, He-enhanced heterogeneity of radiation-induced segregation in FeNiCoCr high-entropy alloy, *J. Mater. Sci. Technol.* 101 (2022) 226–233.
- [15] L.X. Yang, H.L. Ge, J. Zhang, T. Xiong, High He-ion irradiation resistance of CrMnFeCoNi high-entropy alloy revealed by comparison study with Ni and 304SS, *J. Mater. Sci. Technol.* 35 (2019) 300–305.
- [16] D. Chen, Y. Tong, H. Li, J. Wang, Y.L. Zhao, Alice Hu, J.J. Kai, Helium accumulation and bubble formation in FeCoNiCr alloy under high fluence He^+ implantation, *J. Nucl. Mater.* 501 (2018) 208–216.
- [17] D. Chen, Y. Tong, J. Wang, B. Han, Y.L. Zhao, Microstructural response of He^+ irradiated $\text{FeCoNiCrTi}_{0.2}$ high entropy alloy, *J. Nucl. Mater.* 510 (2018) 187–192.
- [18] W.Y. Chen, J.D. Poplawsky, Y. Chen, W. Guo, J.W. Yeh, Irradiation-induced segregation at dislocation loops in CoCrFeMnNi high entropy alloy, *Materialia* 14 (2020) 100951.
- [19] S. Sun, et al., Segregation of $\text{Al}_{1.5}\text{CrFeNi}$ high entropy alloy induced by vacant-type defects, *Scr. Mater.* 161 (2019) 40–43.
- [20] S. Würster, R. Pippin, Nanostructured metals under irradiation, *Scr. Mater.* 60 (2009) 1083–1087.
- [21] I. Beyerlein, A. Caro, M. Demkowicz, N. Mara, A. Misra, B. Uberuaga, Radiation damage tolerant nanomaterials, *Mater. Today* 16 (2013) 443–449.
- [22] X.M. Bai, A.F. Voter, R.G. Hoagland, M. Nastasi, B.P. Uberuaga, Efficient annealing of radiation damage near grain boundaries via interstitial emission, *Science* 327 (2010) 1631–1634.
- [23] G. Pu, L.W. Lin, R. Ang, K. Zhang, B. Liu, B. Liu, T. Peng, S.F. Liu, Q.R. Li, Outstanding radiation tolerance and mechanical behavior in ultra-fine nanocrystalline $\text{Al}_{1.5}\text{CoCrFeNi}$ high entropy alloy films under He ion irradiation, *Appl. Surf. Sci.* 516 (2020) 146129.
- [24] L. Dong, H.X. Zhang, H. Amekura, F. Ren, et al., Period-thickness dependent responses of Cu/W multi-nanolayered nanofilms to ions irradiation under different ion energies, *J. Nucl. Mater.* 497 (2017) 117–127.
- [25] X.Y. Liu, B.P. Uberuaga, M.J. Demkowicz, et al., Mechanism for recombination of radiation-induced point defects at interphase boundaries, *Phys. Rev. B* 85 (2012) 012103.
- [26] H.H. Chen, Y.F. Zhao, J.Y. Zhang, Y.Q. Wang, He-ion irradiation effects on the microstructure stability and size-dependent mechanical behavior of high entropy alloy/Cu nanotwinned nanolaminates, *Int. J. Plast.* 133 (2020) 102839.
- [27] A.P. Sutton, R.W. Balluffi, Interfaces in crystalline materials and surfaces and interfaces of solid materials, *Phys. Today* 49 (1996) 88.
- [28] W.J. Weber, Y.W. Zhang, Predicting damage production in monoatomic and multielemental targets using stopping and range of ions in matter code: challenges and recommendations on the use of SRIM for computing radiation damage exposure, *Solid State Mater. Sci.* 23 (2019) 100757.

- [29] N.A.P. Kiran Kumar, C. Li, K.J. Leonard, H. Bei, S.J. Zinkle, Micro-structural stability and mechanical behavior of FeNiMnCr high entropy alloy under ion irradiation, *Acta Mater.* 113 (2016) 230–244.
- [30] E. Astm, Standard practice for neutron radiation damage simulation by charged-particle, *Annu. B ASTM Stand.* 12 (02) (2009) 1–21.
- [31] G.W. Egeland, J.A. Valdez, S.A. Maloy, K.J. McClellan, K.E. Sickafus, G.M. Bond, Heavy-ion irradiation defect accumulation in ZrN characterized by TEM, GIXRD, nanoindentation, and helium desorption, *J. Nucl. Mater.* 435 (2013) 77–87.
- [32] T.F. Yang, et al., Effects of Al addition on microstructure and mechanical properties of Al_xCoCrFeNi High-entropy alloy, *Mater. Sci. Eng. A* 648 (2015) 15–22.
- [33] C.M. Barr, J.E. Nathaniel II, K.A. Unocic, J.P. Liu, Y. Zhang, Y. Wang, M.L. Taheri, Exploring radiation induced segregation mechanism at grain boundaries in equiatomic CoCrFeNiMn high entropy alloy under heavy ion irradiation, *Scr. Mater.* 156 (2018) 80–84.
- [34] M. Nastar, F. Soisson, Radiation-induced segregation, *Compr. Nucl. Mater.* 1 (2020) 235–264.
- [35] M.R. He, S. Wang, S. Shi, K. Jin, H. Bei, K. Yasuda, S. Matsumura, K. Higashida, I.M. Robertson, Mechanisms of radiation induced segregation in Cr-FeCoNi-based single-phase concentrated solid solution alloys, *Acta Mater.* 126 (2017) 182–193.
- [36] A. Etienne, B. Radiguet, N.J. Cunningham, Comparison of radiation induced segregation in ultrafine-grained and conventional 316 austenitic stainless steels, *Ultramicroscopy* 111 (2011) 659–663.
- [37] T. Nagase, P.D. Rack, J.H. Noh, T. Egami, *In-situ* TEM observation of structural changes in nano-crystalline CoCrCuFeNi multicomponent high-entropy alloy (HEA) under fast electron irradiation by high voltage electron microscopy (HVEM), *Intermetallics* 59 (2015) 32–42.
- [38] S.Q. Xia, X. Yang, T.F. Yang, S. Liu, Y. Zhang, Irradiation resistance in Al_xCoCrFeNi high entropy alloys, *JOM* 67 (2015) 2340–2344.
- [39] K. Durst, B. Backes, M. Göken, Indentation size effect in metallic materials: correcting for the size of the plastic zone, *Scr. Mater.* 52 (2005) 1093–1097.
- [40] H. Ullmaier, The influence of helium on the bulk properties of fusion reactor structural materials, *Nucl. Fusion* 24 (1984) 1039–1083.
- [41] H. Trinkaus, On the modeling of the high-temperature embrittlement of metals containing helium, *J. Nucl. Mater.* 118 (1983) 39–49.
- [42] Z. Di, X.M. Bai, Q. Wei, Tunable helium bubble superlattice ordered by screw dislocation network, *Phys. Rev. B* 84 (2011) 052101.
- [43] K.Y. Tsai, M.H. Tsai, J.W. Yeh, Sluggish diffusion in Co-Cr-Fe-Mn-Ni high entropy alloys, *Acta Mater.* 61 (2013) 4887–4897.
- [44] Y.F. Zh, P.C. Millett, M. Tonks, L.Z. Zh, B. Biner, Molecular dynamics simulations of He bubble nucleation at grain boundaries, *J. Phys. Condens. Matter* 24 (2012) 305005 (12pp).
- [45] A. Kashinath, A. Misra, M.J. Demkowicz, Stable storage of helium in nanoscale platelets at semicoherent interfaces, *Phys. Rev. Lett.* 110 (2013) 086101.
- [46] A. Kashinath, P. Wang, J. Majewski, J.K. Baldwin, Y.Q. Wang, M.J. Demkowicz, Detection of helium bubble formation at fcc-bcc interfaces using neutron reflectometry, *J. Appl. Phys.* 114 (2013) 043505.
- [47] A. Kashinath, M.J. Demkowicz, A predictive interatomic potential for He in Cu and Nb, *Model. Simul. Mater. Sci. Eng.* 19 (2011) 035007.
- [48] H. Schroeder, F.P.F. Paulo, On the coarsening mechanisms of helium bubbles –ostwald ripening versus migration and coalescence, *J. Nucl. Mater.* 179–181 (1991) 1007–1010.
- [49] A. Baldan, Review progress in ostwald ripening theories and their applications to nickel-base superalloys Part I: ostwald ripening theories, *J. Mater. Sci.* 37 (2002) 2171–2202.
- [50] A.E.E. Gruber, Calculated size distributions for gas bubble migration and coalescence in solids, *J. Appl. Phys.* 38 (1967) 243–250.
- [51] H. ATrinkaus, B.N. Singh, Helium accumulation in metals during irradiation – where do we stand? *J. Nucl. Mater.* 323 (2003) 229–242.
- [52] W.R. Tyson, W.A. Miller, Surface free energies of solid metals: estimation from liquid surface tension measurements, *Surf. Sci.* 62 (1977) 267–276.
- [53] P.P. Cao, H. Wang, J.Y. He, C. Xu, S.H. Jiang, J.L. Du, X.Z. Cao, E.G. Fu, Z.P. Lu, Effects of nanosized precipitates on irradiation behavior of CoCrFeNi high entropy alloys, *J. Alloy. Compd.* 859 (2021) 158291.
- [54] Y. Zheng, W. Lu, F. Qian, N. Jia, Y. Dou, X. He, W. Yang, J. Wang, Y. Xue, K. Jin, Self-ion irradiation response of (CoCrFeNi)₉₄Ti₂Al₄ alloy containing coherent nanoprecipitates, *J. Nucl. Mater.* 549 (2021) 152889.
- [55] L. Jiang, Y. Hu, K. Sun, et al., Irradiation-induced extremes create hierarchical face/body centered cubic phases in nanostructured high entropy alloys, *Adv. Mater.* 32 (2020).
- [56] C.L. Xu, X.B. Liu, F. Xue, Y.F. Li, W. Jia, Irradiation-induced BCC-phase formation and magnetism in a 316 austenitic stainless steel, *Nucl. Eng. Technol.* 52 (2020) 610–613.
- [57] C.L. Xu, X.B. Liu, F. Xue, Y.F. Li, Characterization of magnetic properties in a 316 stainless steel after deformation and irradiation, *Fus. Eng. Des.* 133 (2018) 125–129.
- [58] P.R. Okamoto, H. Wiedersich, Segregation of alloying elements to free surfaces during irradiation, *J. Nucl. Mater.* 53 (1974) 336–345.
- [59] S. Choudhury, L. Barnard, J.D. Tucker, T.R. Allen, B.D. Wirth, M. Asta, D. Morgan, Ab-initio based modeling of diffusion in dilute bcc Fe-Ni and Fe-Cr alloys and implications for radiation induced segregation, *J. Nucl. Mater.* 411 (2011) 1–14.
- [60] T.R. Allen, J.T. Busby, G.S. Was, E.A. Kenik, On the mechanism of radiation-induced segregation in austenitic Fe-Cr-Ni alloys, *J. Nucl. Mater.* 255 (1998) 44–58.
- [61] A.D. Marwick, Segregation in irradiated alloys: inverse Kirkendall effect and effect of constitution on void swelling, *J. Phys. F Met. Phys.* 8 (1978) 1849–1861.
- [62] H. Wiedersich, N.Q. Lam, F.V. Nolfi, Theory of radiation-induced segregation, in: *Phase Transformations during Irradiation*, Applied Science Publishers, New York, 1983, pp. 1–46.
- [63] P.R. Okamoto, H. Wiedersich, Segregation of alloying elements to free surfaces during irradiation, *J. Nucl. Mater.* 53 (1974) 336–345.
- [64] A. Janotti, M. Krčmar, C.L. Fu, R.C. Reed, Solute diffusion in metals: larger atoms can move faster, *Phys. Rev. Lett.* 92 (2004) 085901.
- [65] R.A. Johnson, N.Q. Lam, Solute segregation in metals under irradiation, *Phys. Rev. B* 13 (1976) 4364–4375.
- [66] J. Dabrowska, W. Kucza, Interdiffusion in the FCC-structured Al-Co-Cr-Fe-Ni high entropy alloys: experimental studies and numerical simulations, *J. Alloy. Compd.* 674 (2016) 455–462.
- [67] A.J. Ardell, P. Bellon, Radiation-induced solute segregation in metallic alloys, *Curr. Opin. Solid State Mater. Sci.* 20 (2016) 115–139.
- [68] Z. Shang, J. Ding, C. Fan, He ion irradiation response of a gradient T91 steel, *Acta Mater.* 196 (2020) 175–190.
- [69] G. Ayrault, Cavity formation during single- and dual-ion irradiation in a 9Cr-1Mo ferritic alloy, *J. Nucl. Mater.* 114 (1983) 34–40.
- [70] S.J. Zinkle, Y. Matsukawa, Observation and analysis of defect cluster production and interactions with dislocations, *J. Nucl. Mater.* 329–333 (Part A) (2004) 88–96.
- [71] N. Li, M. Demkowicz, N. Mara, Y.Q. Wang, A. Misra, Hardening due to interfacial He bubbles in nanolayered composites, *Mater. Res. Lett.* 4 (2016) 75–82.
- [72] Q.M. Wei, N. Li, N. Mara, Suppression of irradiation hardening in nanoscale V/Ag multilayers, *Acta Mater.* 59 (2011) 6331–6340.
- [73] N. Li, N.A. Mara, Y.Q. Wang, M. Nastasi, A. Misra, Compressive flow behavior of Cu thin films and Cu/Nb multilayers containing nanometer-scale helium bubbles, *Scr. Mater.* 64 (2011) 974–977.
- [74] F. Kroupa, P.B. Hirsch, Elastic interaction between prismatic dislocation loops and straight dislocations, *Discuss. Faraday Soc.* 38 (1964) 49–55.
- [75] Q.Z. Li, P.M. Anderson, Dislocation-based modeling of the mechanical behavior of epitaxial metallic multilayer thin films, *Acta Mater.* 53 (2005) 1121–1134.
- [76] C. Li, J.C. Li, M. Zhao, Q. Jiang, Effect of aluminum contents on microstructure and properties of Al_xCoCrFeNi alloys, *J. Alloy. Compd.* 504S (2010) S515–S518.